Numerical Simulations of Droplet Evaporation and Breakup Effects on Heterogeneous Detonations

Benjamin J. Musick[a], Manoj Paudel[a], Praveen K. Ramaprabhu[b] and Jacob A. McFarland[a,*]

[a]Texas A&M University, College Station, Texas, USA
[b]University of North Carolina - Charlotte, Charlotte, North Carolina, USA

ARTICLE INFO

Keywords:
Multiphase
Droplet
Breakup
Evaporation
n-Dodecane/Oxygen
Detonation
Euler-Lagrange

ABSTRACT

Evaporation and breakup of droplets are critical phenomena in the liquid-fueled, multiphase detonation process. Understanding the relevant conditions and times for each process is crucial for predicting real world behavior. In this paper, the effects of evaporation and breakup on the multiphase detonation process will be explored through Euler-Lagrange (EL) simulations. Various droplet sizes of n-dodecane ($C_{12}H_{26}$) are reacted with oxygen (O_2) utilizing a single-step global reaction mechanism. Droplet processes are modeled using temperature dependent thermophysical properties through the liquid-gas phase change and into the supercritical regime. Two aerodynamic breakup models are considered (based on theorized hydrodynamic instability mechanisms) from both empirical and theoretical approaches. Detonation wave velocity deficits are observed to be sensitive to breakup and evaporation time. It is shown that droplets redistribute fuel vapor mass over their lifetime, perturbing the equivalence ratio and creating vapor rich regions that cannot fully react. It was shown that as the total evaporation time decreases (shorter breakup time), the detonation structure becomes more like the idealized gaseous detonation case.

1. Introduction

Detonations are complex phenomena that involve intricate chemical, heat, and mass transfer processes. Occurring at high speeds, pressures, and temperatures, detonation waves are highly energetic providing an opportunity for higher efficiency in thermodynamic cycles and propulsion devices, as compared to the Brayton cycle [48]. The propagation of detonation waves in gaseous media is well studied but there are many knowledge gaps, particularly in deflagration to detonation transition and wave stability [53]. Further complicating matters, detonations in mixed phases are less studied and characterized. Airborne engines such as Pulse or Rotating Detonation Engines (PDE or RDE) will likely require the use of liquid fuels [77], due to their high density, and thus, will need to consider the complex physics of droplet evaporation and breakup along with accompanying physics of gaseous detonations.

Liquid aviation fuels such as Jet A or JP-5/-8/-10 are likely candidates for PDE and RDE applications [34]. Simultaneous injection, vaporization, and combustion of fuel into such engines requires process control on the order of microseconds. For context, a diesel internal combustion (IC) engine completes these processes on the order of hundreds of microseconds to milliseconds [46]. While the governing processes are understood better in slower combustion systems, the timing required for controlled detonations in fixed, open volumes introduces additional uncertainty. Experimental and, more often, numerical techniques are currently being employed in an attempt to accurately predict

---

*Corresponding Author
mcfarlandja@tamu.edu (J.A. McFarland)
ORCID(s): 0000-0003-0107-3597 (J.A. McFarland)

the conditions seen in detonation engines. The uncertainty in much of the numerical work results from large gaps that exist in current models for the high temperature and pressure conditions seen in a detonation. Droplet combustion models for high temperature and pressure, convective conditions lack validation because of the associated challenges in replicating and adequately measuring such conditions in a laboratory. Kinetic and vaporization models tend to be the most accurate at lower, steady-state temperatures and pressures. The temperatures and pressures seen in a detonation wave front are similar to those in diesel IC engines but the high velocities and highly transient shock wave conditions add to the complexity significantly.

Droplet breakup is often ignored in current analyses despite the fact that it will significantly impact the vapor production process, with predicted droplet breakup times often being less than the evaporation time and on the order of the chemical reaction time scale. There is no well accepted breakup model that sufficiently describes droplet breakup over a wide range of conditions, much less one that incorporates the effects of significant evaporation. There has been considerable work done to discern the individual processes and establish a working breakup theory [23, 71, 88], however, the work is ever changing and still largely incomplete. This previous literature has mostly covered regimes where heat and mass transfer are insignificant and material properties are assumed constant. Under detonation conditions, droplet breakup is different from these previously studied cases since high temperatures will drive material properties such as surface tension to much lower values throughout the process. Further, freestream condition, e.g. velocity and density, change rapidly throughout the breakup. In combination with high free stream temperatures, strong convective forces amplify vaporization through shock acceleration and post shock processing. Quantification of how each mass transfer process contributes to the total evaporation time is important, especially for low vapor pressure fuels where pre-vaporized fuel mass is limited.

Direct Numerical Simulations (DNS) may be capable of predicting droplet evaporation, breakup (e.g., [62, 43]), and detailed chemical kinetics with sufficient accuracy, but the required computational resources are significant and prohibitive at this point. Simplifications are necessary to run full-scale simulations aiming to predict the behavior of detonation engines. Euler-Lagrange (EL) simulations with gas mesh and point-particle droplet representations significantly reduce computational cost and offer a viable alternative to these simulations. This work will provide further insight into the liquid-fueled detonation problem through EL simulations where evaporation and breakup are modeled on the particle points and reactions are modeled on the gas mesh.

1.1. Gaseous and Liquid Fuel Detonations

Most detonation research has focused on homogeneous gas-phase mixtures of fuel and oxidizer, usually a H_2-O_2-Ar media. One-dimensional theory was independently derived by Zel'dovich (Z) [99], von Neumann (N) [91], and Döring (D) [28] that describes a planar, steady detonation (ZND theory). Unfortunately, detonations are unsteady by nature with transverse waves colliding together to form highly complex 3D structures called detonation cells. These cells and their role in the stability of detonation waves, has been the focus of much work, such as experimental work by Pintgen and Shepherd [72]. The 1D ZND model assumes that premixed fuel and oxidizer enter a planar shock wave and are then heated sufficiently to burn completely at finite reaction rate, propelling the shock front. The point at which the local Mach number becomes unity is referred to as the Chapman-Jouget (CJ) Condition or Point [68, 44, 45]. The pressure, temperature, and density at the CJ point along with the detonation velocity are commonly used as metrics to determine the properties of a detonation. In experiments, the approximate CJ pressure and detonation velocity are often the simplest to measure, and are of greater concern for propulsive applications. However, the stable detonation velocity and regular cell size, or lack thereof, are most often reported as metrics for 3D detonations. The cell size is measured using soot foil or optical techniques; correlations exist to predict cell size but there is no strong theory to predetermine cell size [36]. Further, gaseous detonation work from Frolov et al. [33] suggests that experimental initial/boundary conditions like wall geometry or friction can significantly impact the cellular stability of a detonation wave with observable impacts to the measured wave velocity. A detonation velocity with low fluctuations and regular, uniform cells are characteristic of more stable, steady detonations.

In heterogeneous, or multiphase, detonations, the theory becomes more complex and further disrupts the ZND model. A simplified 1D model for fuel droplet combustion has been proposed by Lu and Law [57] and accounts for evaporating particles and heat/friction losses in a detonation tube, however, it does not consider breakup. Instead of premixed gaseous reactants, the leading shock wave propagates through the gas phase containing heterogeneous inclusions from the particle phase. As the shock wave passes over the particles, each will combust on its own time scale, driven by its unique particle properties. Figure 1 provides a visual aid for the liquid-fueled problem. The variation in localized gas and particle conditions leads to heterogeneous conditions that impact the overarching process driving the detonation.

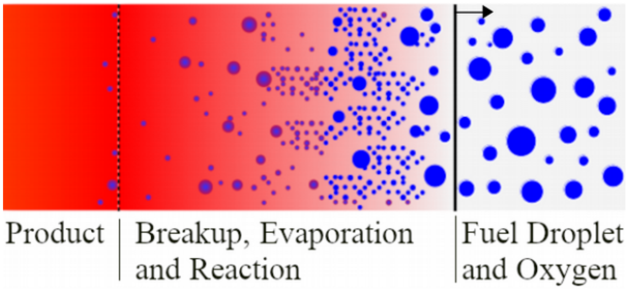

Figure 1: Schematic of a heterogeneous detonation.

While there has been a limited amount of detonation work with liquid hydrocarbon fuels, the existing work shows a highly complex and poorly understood physical process [95, 19, 74, 21, 8, 87, 69, 14, 32, 90, 60, 5, 50, 4].

Kailasanath has provided an overview of the work conducted and the efforts that have been made to refine the theory and working models over the years up to 2012 from both an experimental and numerical point of view [47]. Some of the earliest 1D liquid fuel simulations were conducted by Eildelman and Burcat [29, 12, 30] and Voronin and Zhdan [92] for n-heptane droplet detonations but there is a large gap in time before this topic is revisited again in scientific literature. More recently, there has been an increase in the amount of computational work conducted [15, 83, 90, 5, 4, 81, 80, 51, 39, 42, 63, 64, 100, 55].

Most of these simulations use small droplet sizes, less than 100 μm in diameter, and tend to report small velocity deficits for diameters up to ∼10 μm but report significant deficits or failure when using droplets around 25 or 50 μm in diameter. Experiments have reported results for droplet sizes from 5 μm to 2600 μm. Dabora et al. [21] used diethylcyclohexane (DECH) fuel and reported 4%, 10%, and 26% velocity deficits, as compared to the theoretical CJ velocity for gaseous fuel, for the 290, 940 and 2600 μm droplets. Detonation velocities in fogs and small droplet sprays (below $5 \mu m$) tend to agree with the predicted numerical 1% to 5% deficit but simulations often predict larger velocity deficits or detonation failure in large droplet sprays where detonations have been shown to occur in experiments [15].

The steady-state detonation wave speed is expected to decrease in a liquid-fueled medium compared to the ideal, gaseous detonation. Deficits are usually attributed to the energy required for fuel vaporization or momentum losses, but the exact quantification of this is unclear. Liquid-fueled detonations are heterogeneous by nature and result in spatially perturbed equivalence ratios. Numerical, gaseous detonation studies from Wang et al. [94] and Zhou et al. [101] show that while maintaining a set global equivalence ratio, increasing spatial variation in equivalence ratio will also result in increasing speed deficits. Previous studies [49, 6] of gaseous detonations with transverse fuel concentration gradients have shown a decrease in detonation wave speed compared to homogeneous mixtures with same average concentration. However, other multiphase detonation research has suggested that an increase in detonation velocity is expected either at all or just higher equivalence ratios [70, 83].

1.2. Simulation Considerations

Modeling evaporation for a point particle can be done in many ways. Classic, spherical droplet evaporation consists of a diffusion model between free stream conditions and a droplet surface [20]. Convective mass and heat transfer are modeled using non-dimensional mass transfer coefficient; the Sherwood number, Sh, and the non-dimensional heat transfer coefficient; the Nusselt number, Nu, (defined in Equation 35) to relate the convective to free diffusive mass transfer. Under constant conditions mass transfer follows the the d^2 law; the square of the droplet diameter decreases linearly with time [37]. This model is often lacking due to the transient nature of droplet evaporation and an improved model was provided by Ranz and Marshall [75]. Spalding [85] developed a model based on Ohm's law for high vapor flux and chemically reacting droplets. Further corrections were made by Abramzon and Sirignano [1] to improve model performance under transient conditions with variable thermodynamic properties for sub-critical evaporation of fuel droplets.

In addition to evaporation, droplet breakup is a crucial process to consider because it has a significant impact on the total evaporation time. The time scale for droplet breakup is much shorter than the evaporation time of the parent droplet and likely on the order of the time scale for reaction. The total evaporation time for child droplets may be three to four orders of magnitude less than that of the parent droplet. Breakup characteristics are defined by the Weber number, We, a ratio of inertial to surface tension forces, and breakup is typically assumed to occur for $We > 12$ [71]. Overall, there is a significant lack of data for simultaneous droplet breakup and evaporation, especially at high Weber numbers, $We > 1000$. Breakup models tend to stem from hydrodynamic stability theory [54, 3, 7] or empirical correlations [96, 23, 41]. Recent studies have proposed that the refraction of shock waves within the droplet interior may lead to low pressures sufficient to drive cavitation. Evidence for cavitation has been observed in simplified geometries, a cylindrical interface [82], but recent droplet studies by Dyson et al. [27] and Briggs et al. [10] were not able to obtain any conclusive evidence of cavitation driven breakup and found the breakup morphology similar to that of shear induced (aerodynamic) breakup. While the mechanisms of breakup in detonations remain unproven, evidence from similar high Mach number shock accelerations [26] suggests hydrodynamic instability is likely to play a role. Thus, this work does not include contributions from cavitation in the theoretical breakup model. Regardless of the methods, the models are heavily reliant on physical data and the tuning of parameters. Duke-Walker et al. [24] provide an overview of the development of droplet breakup experiments and models, while more recent work by Duke-Walker et al. [25] examines droplet breakup with rapid evaporation for high We acetone droplets, comparing theoretical and empirical breakup models at these conditions.

After evaporation, the fuel vapor must be combusted to sustain the detonation wave. The broad, gaseous thermochemical process that dictates a reaction in detonation wave is well studied and relatively understood but practical model implementation is often non-trivial. High level details such as kinetic pathways and rates can introduce greater uncertainty. The detailed combustion chemical kinetics, especially of higher/complex hydrocarbons, may not always be well understood since the combination of temperatures and pressures can be much higher than what can be stably reproduced and measured in a laboratory setting. Often, simplifications are made to the reaction chemistry for a reduction in computational cost and complexity. Popular numerical methods used to produce detonations are usually classified by their kinetic modeling approach which can be global, skeletal, or detailed; their ease of implementation lies in the same order. Global and skeletal models are reduced order models from the detailed kinetics that attempt to simplify the chemistry at play while still maintaining realistic behavior. Global mechanisms will be the focus of this study. The work presented here employs a single step Arrhenius rate model progressing reactants to some predefined product composition at an exponential rate. Owing to its simplicity, iterative tuning is required to find model coefficients that provide realistic global features of importance.

The multiphase detonation process is highly dependant on the coupling of mass, momentum, and energy between the carrier and discrete phases. Breakup and evaporation is the driving process fueling the detonation front. Drag forces connect the gas and droplets at a finite rate, allowing for droplet transport, and aiding in the vaporization and breakup process. Heat transfer decreases the temperature of the gas phase due to the latent heat of vaporization, h_{fg}. Heterogeneous droplet spray distributions induce variations in local evaporation conditions. Areas of dry gas promote faster evaporation while those with high droplet volume fractions will evaporate slower due to the abundance of localized vapor. The numerical methods by which the droplet models are coupled to the governing gas flow equations will also have a large impact on simulation results.

1.3. Paper Overview

In this paper, the effects of droplet size, evaporation, and breakup on the propagation of two dimensional n-dodecane/oxygen detonations are explored through numerical simulations. A global, one-step Arrhenius rate reaction is considered for combustion. Droplet heat and mass transfer are considered to follow the methods proposed by Abramzon and Sirignano [1] with improved liquid and gas properties that are temperature, and sometimes pressure, dependant functions. In the base case, droplet breakup will be ignored. Then two breakup models are considered: one based on empirical correlations fit to low We shock tube data first proposed by Wert [96] but later modified [24] and the other based on the hydrodynamic stability theory proposed by Liu et al. [54] and Reitz and Beale [3]. Bulk properties of the detonation are compared to theoretical ZND values for a gaseous equivalent, and the effect of overall evaporation rate and droplet transport considered.

2. Methods

The FLASH hydrodynamics code was employed for the simulations presented in this work; developed in part at the Flash Center for Computational Science [35]. The FLASH code offers features such as Adaptive Mesh Refinement (AMR, PARAMESH [59]) and particle-to-gas property mapping between Euler and Lagrange meshes. More information can be found on the FLASH website.[1]

2.1. Euler-Lagrange Coupling

An approach similar to the Multi-Phase Particle-In-Cell (MP-PIC) method [2, 84] is taken for the implementation of particles. MP-PIC represents particles as Lagrangian points on an Eulerian mesh and interpolates properties between them. The conservation equations for the gas flow and particle motion are solved independently but linked with source

---

[1] https://flash.rochester.edu/site/index.shtml

terms to provide two-way coupling. Past examples of the implementation can be seen in Dahal and McFarland [22] and Duke-Walker et al. [24]. The current implementation includes some improvements, primarily in the method of source term coupling/computation and the evaluation order of the numerical scheme. In the previous work, the particles were first moved to provisional locations and source terms were calculated, next the gas phase was updated with these source terms, and then the particles were advanced with new gas properties. In the present work, the conservation equations are solved without source terms, then particles are advance using sub-stepping (smaller time steps), and finally the source terms are calculated and the gas properties updated.

The gas flow equations for mass, momentum, and energy are expressed in Equations 1, 2, & 3:

$$\frac{\partial \epsilon \rho_g}{\partial t} + \nabla \cdot \epsilon \rho_g \mathbf{v}_g = -M_p \tag{1}$$

$$\frac{\partial \epsilon \rho_g \mathbf{v}_g}{\partial t} + \nabla \cdot \epsilon \rho_g \mathbf{v}_g \mathbf{v}_g + \nabla p = -\mathbf{F}_p \tag{2}$$

$$\frac{\partial \epsilon \rho_g E}{\partial t} + \nabla \cdot (\epsilon \rho_g E + p)\mathbf{v}_g + \frac{p \partial \epsilon}{\partial t} = E_p \tag{3}$$

where the subscripts g and p denote gas and particle properties respectively, ϵ is the gas void fraction, ρ is density, t is time, $\mathbf{v}$ is velocity, p is pressure, and E is energy. M_p , $\mathbf{F}_p$, and E_p (Equations 27 - 29 in Appendix A.1) are the mass, momentum, and energy source terms from the particle phase respectively. Reaction energy source terms are not incorporated into the flow equations since changes in species composition are handled by the curve fit thermodynamics employed in the EOS, and thus, capture the changes in temperature associated with reactions. Tracking multiple species in our simulation with some that evaporate and others that react requires the addition of Equation 4:

$$\frac{\partial \epsilon \rho_g Y_i}{\partial t} + \nabla \cdot \epsilon \rho_g Y_i \mathbf{v}_g = -M_{p,i} + \dot{\omega}_{rxn,i} \ , \quad \sum_{i=1}^{n} Y_i = 1 \tag{4}$$

where Y is mass fraction, $\dot{\omega}_{rxn}$ is the reacting species mass consumption or production rate, and the subscript i represents each species in the simulation. $M_{p,i}$ and $\dot{\omega}_{rxn}$ are zero for non-evaporating and non-reacting species, respectively. The gas equations are solved in a finite volume approach using directional splitting and a higher-order Godunov method (PPM [18]) for data reconstruction which yields good accuracy at discontinuities.

The Lagrangian particle system is solved using the Liouville equation for the particle distribution function, h, as seen in Equation 5:

$$\frac{\partial h}{\partial t} + \nabla \cdot (h\mathbf{v}_p) + \nabla \mathbf{v}_p \cdot (h\mathbf{a}_p) = 0 \tag{5}$$

where $\mathbf{a}_p$ is the acceleration of the particles and is given by Equation 6:

$$\mathbf{a}_p = \frac{d\mathbf{v}_p}{dt} = \mathrm{f}_D(\mathbf{v}_g - \mathbf{v}_p) - \frac{1}{\rho_p}\nabla P \tag{6}$$

For this study, the particle volume fraction is relatively low so inter-particle stress terms are neglected. Additionally, gravity for both gas and particle motion is not incorporated as its contribution would be negligible over the time scales considered here. The scalar drag component, f_D, is evaluated as seen in Equation 7:

$$\mathrm{f}_D = C_d \frac{3}{8} \frac{\rho_g}{\rho_p} \frac{|\mathbf{v}_g - \mathbf{v}_p|}{r_p} \tag{7}$$

where C_d is the coefficient of drag and r_p is the current particle radius. We consider two different models for the calculation of C_d for non-deforming and deforming particles as explained in Section 2.2.

More accurate results are achieved when each Lagrangian point represents a single particle but this becomes computationally taxing for small droplets, where many more are needed for a given equivalence ratio. To circumvent this problem, we give each Lagrangian point a parcel size, N_p, i.e. if a point has the attributes D=10 μm and $N_p = 100$, it will represent 100 particles with a 10 μm diameter at the singular point. If the particle field were viewed as a continuous fluid, then the number of Lagrangian points can be viewed as the resolution of this field. This resolution affects the gas-phase resolution of the particle source terms, and if it is not sufficient it will result in deleterious effects [61, 24]. At a minimum, one particle point must be present in every gas zone to resolve the source terms, here we have used an average of four.

Gas properties are mapped to the particle location and particle properties to the gas mesh using bilinear interpolation in 2D. Once the particle properties are updated, the change in mass, momentum, and energy of individual particles is calculated and mapped to the gas mesh and constitutes the source terms. Equations for calculation of source terms and update algorithm are provided in Appendix A.1.

2.2. Drag Models

For a non-deforming, spherical particle, the coefficient of drag is determined from Equation 8:

$$C_{d,sph} = \begin{cases} \frac{9}{2}\frac{\mu_{g,\infty}}{r^2\rho_p} & Re \leq 0.1 \\ \frac{24}{Re}(\epsilon^{-2.65} + \frac{Re^{2/3}}{6}\epsilon^{-1.78}) & 0.1 < Re < 1000 \\ 0.424 & 1000 \leq Re \end{cases} \tag{8}$$

where $\mu_{g,\infty}$ is the free-stream dynamic viscosity and Re is the Reynolds number evaluated at the free stream conditions, $Re = \rho_{g,\infty}|\mathbf{v}_g - \mathbf{v}_p|2r_p/\mu_{g,\infty}$. Deformation is calculated by solving the second order equation for droplet surface oscillation as given by the TAB model [67], Equation 9:

$$\frac{d^2y}{dt^2} = \frac{C_f\rho_g|\mathbf{v}_g - \mathbf{v}_p|^2}{C_b\rho_p r_p^2} - \frac{C_k\sigma}{\rho_p r_p^3}y - \frac{C_\delta\mu_p}{\rho_p r_p^2}\frac{dy}{dt} \tag{9}$$

where y is the non-dimensional deformation equal to $x/(C_b r_p)$ (x = displacement of droplet equator from its undisturbed position), C_f, C_k, C_b and C_δ are constants, μ_p is the liquid dynamic viscosity and σ the liquid surface tension. Based on the calculated deformation, the coefficient of drag is evaluated as the weighted average of a non-deforming sphere and a disk (see Appendix A.5 for more).

2.3. Evaporation Model

For droplet heat and mass transfer the approach presented by Abramzon and Sirignano [1] is used. Mass transfer is calculated as

$$\begin{aligned} \dot{m} &= 2\pi\bar{\rho}_g\bar{D}_g r_p Sh^* \ln(1 + B_M) \\ \dot{m} &= 2\pi\frac{\bar{k}_g}{\bar{C}_{p,f}} r_p Nu^* \ln(1 + B_T) \end{aligned} \tag{10}$$

where D is the diffusion coefficient, k is the thermal conductivity, $C_{p,F}$ is the fuel vapor heat capacity, and the over line (e.g., $\bar{\rho}$) signifies film properties, a weighted average between the surface and free stream conditions (see Equation 36 in Appendix A.2). Sh^* is the modified Sherwood number, Nu^* is the modified Nusselt number, and B_M & B_T are the Spalding mass and heat transfer numbers.

The Spalding mass and heat transfer numbers are calculated according to Equation 11:

$$B_M = \frac{Y_{F,s} - Y_{F,\infty}}{1 - Y_{F,s}} \quad , \quad B_T = \frac{\bar{C}_{p,F}(T_\infty - T_s)}{L(T_s) + Q_L/\dot{m}} \tag{11}$$

where Y is fuel mass fraction, T is temperature, L is the latent heat of vaporization calculated at the specified temperature, Q_L is the heat transfer into the droplet, and subscripts s and ∞ designate surface and free stream properties, respectively. The complete solution procedure can be seen in Appendix A.2.

It is possible that a portion of droplet evaporation occurs at supercritical conditions in an oxygen or oxygen enriched detonation front because of the increased temperatures. Qualitatively, we can assess that supercritical evaporation is most likely dominated by diffusion. While DNS of supercritical droplets has been performed [9], neither a general solution for the superciritical diffusion rates nor zero-dimensional evaporation model for supercritical conditions is readily available. Our model limits the droplet temperature to the critical temperature, so that heat transferred from the gas phase is used exclusively to convert supercritical liquid mass to vapor at the free stream conditions. The vapor production rate is calculated from Equation 10, considering a maximum vapor surface mass fraction, $Y_{F,s}$, of 0.99 for the calculation of B_M (Equation 11). This results in a diffusion limited process and provides a high mass transfer rate throughout the critical vaporization time.

2.4. Breakup Models

After heat and mass transfer has been calculated, the simulation then advances to breakup evaluation. Breakup characteristics are defined by the Weber number, $We = \rho_g |\mathbf{v}_g - \mathbf{v}_p|^2 2r_p/\sigma$, with different morphologies and breakup times observed at different We ranges. Ranger and Nicholls [66] proposed a dimensionless breakup time for characterizing breakup events, as seen in Equation 12:

$$\tau = t\left(\frac{v_{g,i}}{2r_{p,i}}\right)\sqrt{\frac{\rho_g}{\rho_p}} \tag{12}$$

where t is the time since the droplet was exposed to breakup conditions, $v_{g,i}$ is the initial relative velocity (e.g. post shock velocity), and $r_{p,i}$ is the initial droplet diameter. The value of this non-dimensional time at the point of breakup completion is referred to as the characteristic breakup time ($\tau_{brk,f}$). Another important event is the breakup initiation time ($\tau_{brk,i}$), the time required for deformation and onset of breakup. Other models may describe these events in terms of the active modes of breakup, such as times corresponding to Kelvin-Helmholtz (KH, $t_{brk,KH}$) or Rayleigh-Taylor (RT, $t_{brk,RT}$) instability modes.

We utilize two models, one empirical (WERT49) and the other theoretical (KHRT). The empirical model calculates breakup conditions based on the highest relative velocity observed by the particle. The final child droplet radius ($r_{c,f}$) is calculated from Equation 13 where We_{brk} is the Weber number corresponding to the highest droplet relative velocity, and $\tau_{brk,i}$ (typically ~1) and $\tau_{brk,f}$ (typically ~4-6.) are calculated from eqns 47 and 48 in appendix A.3.

$$r_{c,f} = 0.49We_{brk}[\tau_{brk,f} - \tau_{brk,i}]^{2/3}\frac{\sigma}{2|\mathbf{v}_g - \mathbf{v}_p|^2\rho_g} \tag{13}$$

After $\tau_{brk,i}$ time has passed, the parcel size of the Lagrangian point exponentially increases until the final child size is achieved at $\tau_{brk,f}$. The empirical model coefficients are tuned with previous experimental measurements for shock-driven problems as explained in Duke-Walker et al. [24]. The complete algorithm can be seen in Appendix A.3. The empirical model yields good agreement with experimental results [24], but does not have a complete theoretical background. Further, works such as Theofanus & Li [89] suggest that the catastrophic breakup regime does not exist and that the breakup times are much shorter than what is calculated by this model. The WERT49 model predicts non-dimensional breakup times in the range of $\sim 4-6$ while Theofanus & Li [89] claim realistic times are closer to one.

The KHRT model has an analytical background, but uncertainty remains in the coefficients of choice. Based largely on the work of Reitz [76], Su et al. [86] and Beale & Reitz [3], this model is founded in KH and RT hydrodynamic instability theory and was originally tuned for diesel spray combustion. Here we use the coefficients of Beale & Reitz [3].

$$\Lambda_{KH} = \frac{9.02r_p(1+0.45\sqrt{Oh})(1+0.4Ta^{0.7})}{(1+0.865(We/2)^{1.67})^{0.6}} \tag{14}$$

$$\Omega_{KH} = \frac{0.34+0.38(We/2)^{1.5}}{(1+Oh)(1+1.4Ta^{0.6})}\sqrt{\frac{\sigma}{\rho_g r_p^3}} \tag{15}$$

$$r_{c,KH} = B_0\Lambda_{KH} \tag{16}$$

For the KHRT model, a parent droplet of radius, r_p, will strip child droplets of size $r_{c,KH}$ due to KH instabilities according to Equations 14-16, where Λ_{KH} is the KH wavelength with the maximum growth rate (frequency), Ω_{KH}. The Ohnesorge number, Oh, quantifies the effects of droplet viscosity and is expressed as $\mu_p/\sqrt{2r_p\rho_p\sigma}$, where μ is the dynamic viscosity. The Taylor number, Ta, is computed as $Oh\sqrt{We}$.

The rate of change of the parent droplet radius can be expressed as seen in Equation 17:

$$\frac{dr_p}{dt} = \frac{r_p - r_{c,KH}}{t_{brk,KH}} \tag{17}$$

where $t_{brk,KH}$ is the KH breakup time in seconds given by Equation 18.

$$t_{brk,KH} = \frac{3.726 B_1 r_p}{\Omega_{KH} \Lambda_{KH}} \tag{18}$$

The KH model sheds child particles that are spawned as new Lagrangian points next to the parent droplet assuming that the properties of the child are the same as the parent with the exception of radius and parcel size. The parcel size is determined by the child droplet radius and the mass shed by the parent between time steps. The KH model will generate child droplets until the droplet either evaporates, reaches its final KH breakup time, or is terminated by RT breakup.

The RT instability evolves simultaneous to the KH instability. For the RT model, the frequency of the fastest growing wave and the wavelength of the fastest growing wave are provided in Equations 19 and 20, where g_t is the acceleration of the droplet in the direction of travel (given by $g_t = \mathbf{a}_p$, see Equation 6), evaluated at the breakup initiation time.

$$\Omega_{RT} = \sqrt{\frac{2}{3\sqrt{3\sigma}} \frac{[-g_t(\rho_p - \rho_g)]^{1.5}}{\rho_p + \rho_g}} \tag{19}$$

$$\Lambda_{RT} = 2\pi C_{RT} \sqrt{\frac{3\sigma}{-g_t(\rho_p - \rho_g)}} \tag{20}$$

For both KH and RT models, the calculated wavelength must be smaller than the droplet diameter or breakup will be prevented. The RT breakup time ($t_{brk,RT}$) and final child droplet radius ($r_{c,RT}$) are evaluated as seen in Equations 21 and 22.

$$t_{brk,RT} = \frac{C_\tau}{\Omega_{RT}} \tag{21}$$

$$r_{c,RT} = \frac{\Lambda_{RT}}{2} \tag{22}$$

If the droplet reaches the RT breakup time, the parent Lagrangian point is modified so the radius is set equal to the calculated RT child droplet size and the parcel size is adjusted to conserve mass. Both breakup mechanisms are recalculated if the parent radius decreases below the initially calculated child radius, resulting in a new breakup process if the droplet conditions remain unstable. The entire solution procedure can be seen in Appendix A.4. The values of adjustable constants B_0, C_{RT} and C_τ in the KHRT model are taken from [3] and are equal to 0.61, 0.1 and 1. The value of B_1 is taken from [54] and is equal to 1.71. Using this value for B_1 gives characteristic breakup times on the order of 1, which are suggested to be the most realistic by Theofanous and Li [89].

2.5. Thermophysical Properties of Fuel

The straight-chain alkane n-dodecane has been selected as the fuel for the following simulations. Choosing a pure fuel is advantageous from a numerical point of view because there is less uncertainty when evaluating fuel properties. From an application standpoint, n-dodecane is often used as a surrogate for jet-fuel blends, which often contain some percentage of $C_{12}H_{26}$ in their composition. There is much less work done for dodecane and other low vapor pressure hydrocarbons in detonations compared to other fuels, e.g. heptane (high vapor pressure) is commonly used in experiments and simulations. The experimental and simulation work that does exist for low vapor pressure fuels suggests very unstable detonation regimes, if not failures to detonate, requiring either a high initiation energy or a degree of prevaporization for sustained waves [5, 60, 51, 11, 78].

The liquid phase properties of n-dodecane are correlated from data provided by the National Institute of Standards and Technology (NIST, see Appendix B.1 for correlations). The gas phase species are assumed to behave as ideal gases with enthalpy correlations given by NASA7 polynomials. For consistent evaluation, the liquid enthalpy was referenced at 298.15 K to the vapor enthalpy using the latent heat of vaporization. The vapor enthalpy was taken to be that of an ideal gas found from the NASA7 polynomial correlation. The resulting T-h diagram is shown in Figure 2. Representing the vapor phase as an ideal gas results in an enthalpy departure from the vapor (real gas) near the transcritical region as seen in T-h diagram. The largest deviation of ideal gas enthalpy from saturated vapor enthalpy is seen at critical point and is ~14.8%, only rising above 5% at temperatures above 625 K. Evaporation models typically assume that the energy require to overcome the latent heat of vaporization is acquired from the droplet mass. Here we calculate the latent heat as the difference between the compressed liquid and ideal gas enthalpies at the droplet temperature ($h_{fg}(T) = h_{g,ideal}(T) - h_l(T)$). This has the advantage of accounting for the additional boundary work required to change from a compressed to a saturated liquid and from a saturated vapor to and ideal gas, once expanded to its free stream partial pressure. While it would be more consistent with previous models to acquire the ideal gas boundary work from the free stream gas, the best method in the transcritical regime remains to be determined. Furthermore, this method was deemed the most consistent from both a numerical and thermodynamic standpoint, avoiding severe mismatches in energy calculations, and allowing for easy energy communication between the gas mesh and particle point.

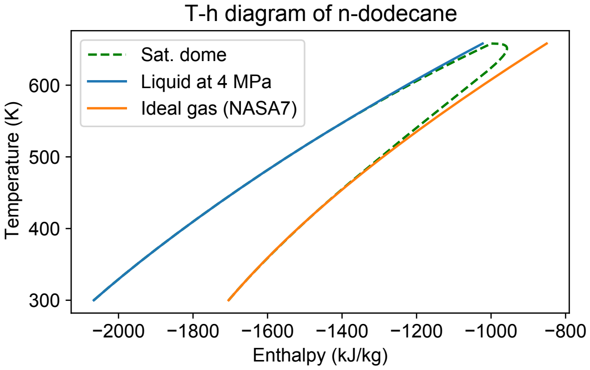

Figure 2: Enthalpy variation of liquid and gas n-dodecane

2.6. Reaction Model

A one step irreversible reaction is employed in the gas phase where n_f moles of fuel react with n_o moles of oxygen to give n_p moles of product ($n_f F + n_o O_2 \rightarrow n_p P$). The overall reaction rate is given in Arrhenius form as:

$$k_{ov} = -\frac{1}{n_f}\frac{d[F]}{dt} = -\frac{1}{n_o}\frac{d[O_2]}{dt} = \frac{1}{n_p}\frac{d[P]}{dt} \tag{23}$$

$$k_{ov} = A \cdot exp\left(-\frac{E_a}{R_u T}\right)[F]^a[O_2]^b \tag{24}$$

where A is the pre-exponential factor, E_a is the activation energy, $[N]$ denotes molar concentration of species N, and a and b are chosen constants for irreversible reactions. The fuel consumption rate defined in Equations 23 and 24 can also expressed in terms of mass fractions as seen in Equation 25.

$$\frac{dY_f}{dt} = -\frac{n_f}{MW_f^a MW_o^b}\rho^{(a+b)}A \cdot exp\left(-\frac{E_a}{R_u T}\right)Y_f^a Y_o^b \tag{25}$$

Thermodynamic properties of the singular product species are taken as a mixture of the seven most abundant species present at the CJ point for stoichiometric burning conditions; equivalence ratio (ϕ) of 1. The equilibrium calculation used a full species list from detailed chemistry. The relevant detonation conditions for the stoichiometric mixture were predicted with the SD Toolbox Cantera plug-in using the JetSurF 2.0 chemical kinetics mechanism [38, 52, 93]. The molecular weight and heat capacity of the product species is determined from the ideal gas assumption of molar/mass fraction averaged properties, which gave a product molecular weight of 23.1707 [g/mol]. The product composition is specified in Appendix B.4. The reaction molar balance is then given as $C_{12}H_{26} + 18.5O_2 \rightarrow 32.9P$.

No single-step reaction rate will be able to fully replicate the real combustion process but for any practical detonation simulation key macroscopic features like the CJ-speed (D_{CJ}), induction times and cell width are recovered with acceptable error. Constants (A, E_a, a, b) were determined such that the reaction rate reproduces the peak thermicity length or half reaction length found in a ZND simulation (see Figure 3) and the effective activation energy(θ) in a constant volume explosion with acceptable agreement to Cantera/SDToolbox results utilizing the detailed JetSurF 2.0 mechanism. The effective activation energy is calculated using Equation 26 following Schultz and Shepherd [79].

$$\theta = \frac{1}{T_{vN}} \frac{ln(t_1) - ln(t_2)}{1/T_1 - 1/T_2} \tag{26}$$

In Equation 26, T_1 and T_2 are temperatures 1% below and above the von-Neumann temperature (T_{vN}) and t_1 and t_2 are the corresponding induction times taken to be equal to the peak thermicity time (time corresponding to peak thermicity length). E_a is taken from Horning [40]. Constants a and b are chosen to get a reaction order of 1.75 (as suggested by Westbrook and Dryer [97]) while exibiting increasing induction times with decreasing equivalence ratio in a constant volume explosion for high pressure and temperature conditions (as given by JetSurF2.0). The single step reaction parameters are presented in Table 1.

Table 1
Single Step Reaction Rate Parameters

$E_a(cal/mol)$	a	b	A
46500	1.0	0.75	6.6E13
Species	O_2	$C_{12}H_{26}$	P
Molecular Wt.	31.9988	170.3348	23.1707

Table 2 shows the comparison of CJ speed and gas properties at the CJ point calculated in SD Toolbox using JetSurF2.0 and the single-step global mechanism. The value of θ is calculated using Equation 26 and is found to be close to the value obtained using JetSurF2.0, but, if the simple relation $E_a/(RT_{vN})$ is used, it gives a higher value of

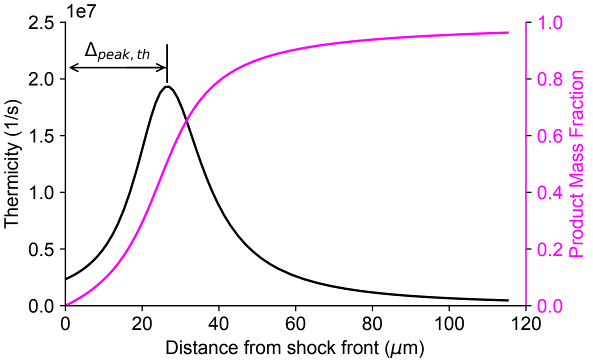

Figure 3: ZND profile for single step mechanism showing the thermicity and product mass fraction behind the wave, calculated using SD Toolbox

Table 2
n-Dodecane/Oxygen Detonation Properties for $\phi = 1.0$, calculated using SD Toolbox (SD-T) and FLASH (1D)

Parameters	JetSurF2.0 (SD-T)	Single Step (SD-T)	Deviation (%)	FLASH (Single Step)	Deviation (%)
D_{CJ} [m/s]	2336.5	2336.6	0.004	2335.2	-0.05
P_{CJ} [MPa]	4.126	3.959	-4.05)	3.97	-3.78
T_{CJ} [K]	3870.8	3851.4	-0.5	3853	-0.46
ρ_{CJ} $[kg/m^3]$	2.966	2.865	-3.41	2.87	-3.24
$\Delta_{peak,th}$ [μm]	26.9	27	0.37	-	-
$t_{peak,th}$ [s]	1.01×10^{-7}	1.043×10^{-7}	3.26	-	-
θ	8.07	8.1 (12.05)	0.37	-	-

12.05. The results of the single-step mechanism are within an error of 1% except for P_{CJ} and ρ_{CJ} which deviate by around 4%.

3. Simulation Setup and Verification

The domain of interest is a straight, rectangular shock tube as seen in Figure 4. The domain y-direction width was chosen to be 5.715 cm to match a known laboratory setup in anticipation of future experimental comparisons [98]. The length of the domain was set to be 114.3 cm to give the simulation adequate time to develop into steady-state conditions while providing square zones. All boundary conditions for the Euler equations were specified to be no-penetration, reflecting walls to match shock tube conditions. Time stepping was capped at a maximum value of 2 nanoseconds per cycle.

Detonation initiation was facilitated through four circular pockets of high temperature (2000 K) and pressure (10 atm) initialized near the left wall. For multiphase simulations, the location of the droplet seeded region ranged from 10 cm to the end of the domain. Initiating the heterogeneous detonation with a gaseous detonation was a quick, consistent way (numerically) to initiate the multiphase detonation and obtain steady results. This method is not unlike

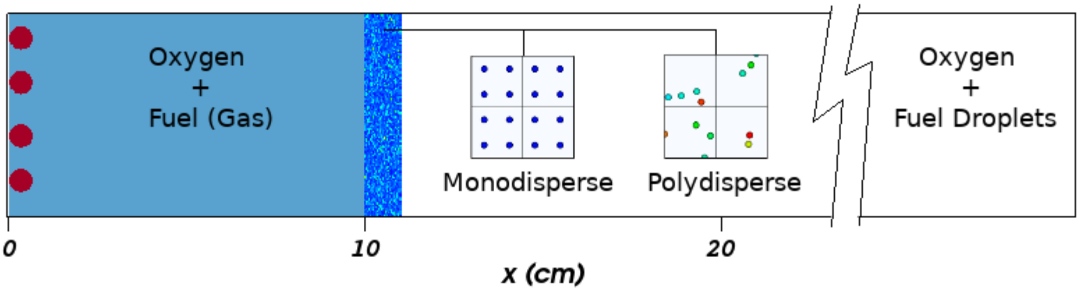

Figure 4: Domain setup for the problem of interest. A 114.3 $cm \times 5.715\ cm$ rectangle was used for the 2D dimensional cases.

experimental methods, where gaseous fuels are used to promote rapid transition to detonation, and usually ensures the formation of a detonation wave [87, 4].

3.1. Gaseous Detonation Verification

Table 2 shows the gaseous detonation speed and CJ properties obtained from 1D simulation with the single step mechanism in FLASH using a mesh size of $223\mu m$. The deviation from Cantera using a full mechanism is less than 5% for all parameters.

Table 3
Detonation speed for different mesh sizes in 2D

Parameters	446 μm	223 μm	112 μm	56 μm
D_{CJ} [m/s]	2354.74	2369.6	2369.4	2373.2

The wave speed in 2D was calculated by tracking the location of the wave front in the centerline of the domain. Although the speed fluctuates in time, the average speed over time approaches a constant value of 2369 m/s, a deviation of +1.4 % from the 1D simulation. Looking at the speed obtained with different mesh sizes (see Table 3) we see that increasing the mesh resolution above 223 μm does not have a large impact on the average speed

For the particle in cell approach, it is generally accepted that particle size must be much lower than the grid size. Luo et al. [58] states that the grid size should be ten times the particle diameter if local gas temperature is used for the prediction of evaporation. Given that we use a bilinear interpolation for particle properties, accessing gas properties (e.g. temperature) from a four zone area, a factor of five was used instead to determine our particle size limit here. Considering the mesh size restriction imposed by the PIC method, the $223\mu m$ mesh size was deemed sufficient for understanding the effect of droplet breakup models; the goal of the present paper.

3.2. Initial conditions for particle simulations

2D simulations with both monodispersed (uniform size and uniform spatial distribution) and polydispersed (lognormal size and random-uniform spatial distribution) particles were run with a global equivalence ratio(ϕ) of 1. For monodispersed cases, four particles per smallest gas mesh were initialized giving a total of 4,784,128 particle points in the domain, while for the polydispersed case the number of points varied by droplet size. The particles were initialized ahead of the shock front at runtime in a rolling window (as particle points completely evaporate, new point are initialized upstream) to save the computational time. The window was maintained such that the distance between furthest un-shocked particle and shock front was always greater than $2.5mm$. The parcel size was set to ensure $\phi = 1$ was obtained. A spray with a lognormal diameter distribution was chosen because most nozzles produce droplets distributed similarly. This distribution is also beneficial from an implementation perspective since choosing two parameters, e.g. $D_{50\%}$ & σ or D_{10} & D_{32}, pins down all of the relevant spray characteristics that can be compared commonly reported nozzle distribution data such as D_{10}, D_{20}, D_{30}, D_{32}, and D_{43}. The Lagrangian points were spawned in the same locations with the same sizes for each breakup model at a single droplet size.

Given the particle-to-mesh size limitation discussed earlier, the 223 μm mesh size required the use of a 45 μm diameter cutoff size. For the diameter distributions (μ and σ) chosen in this study, the truncated distribution captured 90% (largest μ) or more (medium and small μ) of the mass associated with the original log-normal distribution. This ensured that the truncation did not change the initial clustering and liquid mass distribution in the domain. The parameters for both the monodispersed and polydispersed droplet cases simulated can be seen in Table 4.

4. Results

First, droplet lifetimes will be examined under idealized 1D shock conditions to provide context for the 2D simulations. Then, results of the 2D simulations with monodispersed particles will be presented followed by the results of polydispersed cases. The purpose of first examining monodispersed droplets is to obtain insight into the effect droplet size alone has on the detonation wave. Since such cases are unrealistic, lognormal diameter and random-uniform spatial distributions will be studied next to provide results that may be compared more easily with experimental data. For all

Table 4
Parameters for particles sizes and parcel used for multiphase simulations

Monodispersed			**Polydispersed**					
Size [μm]	N_p	points	Distribution	D_{10} & D_{32} [μm]	μ	σ	N_p	points
5	959	4784128	Small	5 & 10	-8.467336	0.588705	400	4100555
10	120	4784128	Medium	10 & 18	-7.747849	0.542119	63	4022249
20	15	4784128	Large	20 & 27	-6.973346	0.362191	12	4314191

results, the deviation of the detonation speed and cellular structure will be compared to the gaseous detonation baseline case. The root cause of such deviations will be explored and the potential explanations will be presented.

4.1. Droplet Lifetime

Before 2D detonation results are examined, it is useful to consider the breakup and evaporation processes in isolation, to understand their role in vapor production and subsequent combustion. To highlight the effects of breakup and evaporation under strong shock conditions, 1D simulations were carried out for single droplets under the post shock conditions of gaseous oxygen obtained with the shock wave speed equal to the gaseous CJ speed (2336 m/s). The droplets were allowed to breakup and evaporate without considering reaction. As seen in Table 5, the inclusion of a breakup model reduced the total time for evaporation by two to four orders of magnitude. In the case of a 20 μm droplet, the evaporation time went from fractions of a millisecond to 1.48 μs and 72 ns with the WERT49 and KHRT models, respectively. As previously mentioned, it was hypothesized that under such conditions the droplets may reach the critical point. These 1D studies revealed that droplet lifetime is long enough, heat transfer rates are high enough, and free stream conditions are sufficiently elevated to bring the droplets to the critical point. This occurs at late times for droplets with no breakup model but only after breakup and for child droplets in the Wert49 and KHRT models. Without breakup over 50% of mass transfer took place after droplet reached critical temperature. When breakup was considered, the break up occurred before critical temperature was reached and it was the child droplets (each with less than 1% of total mass of parent droplet) that reached critical point.

Table 5
Droplet Lifetime with different breakup models (shock speed = 2336 m/s)

Breakup Model	D_p (μm)	t_{evap} (s)	t_{evap}/t_{th}
No Breakup	5	1.77E-5	169.6
	10	6.69E-5	641.4
	20	2.57E-4	2464
WERT49	5	3.04E-7	2.91
	10	6.04E-7	5.79
	20	1.48E-6	14.2
KHRT	5	2E-8	0.192
	10	4.2E-8	0.42
	20	7.2E-8	0.69

For comparison to reaction time scales, the ratio of the evaporation (in absence of reactions), t_{evap}, to peak thermicity time (for gaseous ZND simulation), $t_{th,peak}$, is presented. With the KHRT breakup model, all the simulated droplets completely evaporate before the peak thermicity time, while in the absence of breakup, evaporation takes hundreds to thousands of times longer. This makes it clear that the inclusion of a breakup model will significantly impact the availability of gaseous fuel and thus the total time of reaction in multiphase detonations. Altogether, the order

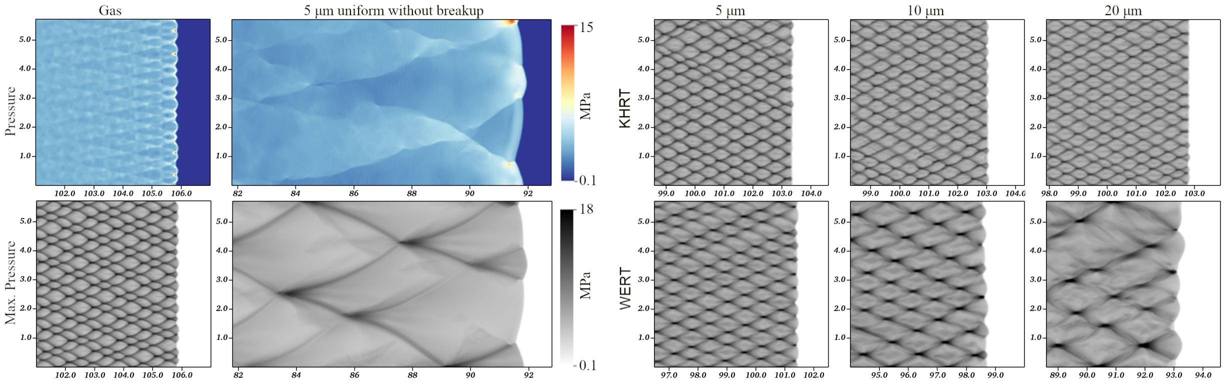

Figure 5: Pressure profiles and numerical soot foils showing detonation cells for gas only and monodispersed particles without breakup (left and middle) and soot foils for monodispersed particles with breakup (right). All at 450 μs

of magnitude for each process is expected to be $\mathcal{O}(10^{-8}[s])$ for characteristic breakup [66], $\mathcal{O}(10^{-5}[s])$ for evaporation without breakup, and $\mathcal{O}(10^{-7}[s])$ for the gaseous reaction length scale.

4.2. Monodispersed Particles

The case of 2D detonations into monodispered, uniformly spaced droplets is now considered. As the detonation, initiated in the gas-phase fuel and oxidizer transition to the particle region, the absence of pre-vaporized fuel causes it to slow down. As significant droplet vapor production begins, the detonation wave speed climbs again. Similar to the gaseous case, the speed is never constant, but with sufficient time it reaches a constant average value (D_{CJ}). The average speed is seen to be lower than the gaseous case in all particle cases with the deficit depending on the droplet size and breakup model, see Table 6. At a minimum, a small deficit must occur due to the energy required (latent heat) for vaporization of the droplet mass.

Table 6
2D Detonation Results for Monodispersed Particles

Breakup Model	Size, D_p μm	Speed (m/s)	ϵ_{gas} (%)	Cell Size (mm)
None	5	2033.45	-14.18	28.58
WERT49	5	2298.2	-3.01	5.2
	10	2259.4	-4.65	8.2
	20	2152.1	-9.17	12.7
KHRT	5	2310.7	-2.48	4.4
	10	2307.4	-2.62	4.76
	20	2309.5	-2.54	4.76

The largest drop in speed is seen in the case without breakup; 5μm droplets without breakup show a larger deficit than 20μm droplets with breakup. Further, the detonation cells are also much larger when breakup is not considered. Neither a steady wave speed or regular cellular structure were observed for 10 μm droplets without breakup. The detonation wave does not recover for 20 μm droplets without breakup and results in a detonation failure. The WERT49 breakup model gives a monotonous decrease in wave speed with increasing droplet size. In contrast to the WERT49 model, the wave speed of the KHRT model is insensitive to the droplet sizes considered and cell sizes are comparable to the gaseous detonation case, see Figure 5. It would appear that droplet lifetime dictates these observed effects and, as discussed in Section 4.1, vapor production is much faster with the inclusion of a breakup model. Since the KHRT model produces much smaller child droplets at a faster rate, complete vaporization is achieved before the induction time of premixed reactants. The result is essentially a gaseous detonation with the deficit being primarily due to the latent heat of vaporization.

It is generally accepted that the detonation speed is influenced by the degree of combustion completion at the sonic plane [31] and cell size is correlated to the reaction rate, or length of the reaction zone, giving larger cells for slower rates and longer reaction zones [36]. For KHRT breakup, the vapor production rate is faster, thus so is the reaction, giving similar cell sizes to that of the gaseous case. But for WERT49 breakup, the reaction time increases for larger droplets due to the longer breakup time, and thus the cell size increases with the droplet size.

To better understand the reasons behind the varying degree of deficit in speed for different droplets sizes and breakup models, the interactions occurring behind the detonation front need to be explored. It is known that disturbances beyond the sonic plane do not affect the detonation front. The sonic plane, i.e. regions with relative (in the detonation reference frame) Mach numbers equal to 1, is not well defined in 2D and 3D simulations because there are pockets of subsonic and supersonic regions appearing and disappearing throughout the simulation. Nevertheless, an approximate sonic plane location can be determined by averaging the properties in the y-direction (parallel to the wave front) and plotting the Mach number in the x-direction (normal to wave front). Figure 6 shows the average Mach number plot for a case without breakup. Here, looking at the particle positions in Figure 6, it can be seen that the particles do not lag behind the sonic plane but are completely vaporized far in advance of it. Regions of uncombusted vapor are observed in and around the sonic plane, potentially suggesting that a significant portion of vapor leaves the sonic plane without contributing to the detonation.

Table 7
Sonic length and Parameters at Sonic Plane for Monodispersed Particles

Breakup Model	D_p	x_{ds} (cm)	$Y_{p,avg}$	σ_ϕ
None	5	3.862	0.82	0.45
WERT49	5	3.26	0.983	0.044
	10	4.33	0.97	0.077
	20	4.6	0.93	0.21
KHRT	5	1.92	0.996	0.012
	10	2.59	0.995	0.01
	20	2.21	0.994	0.014

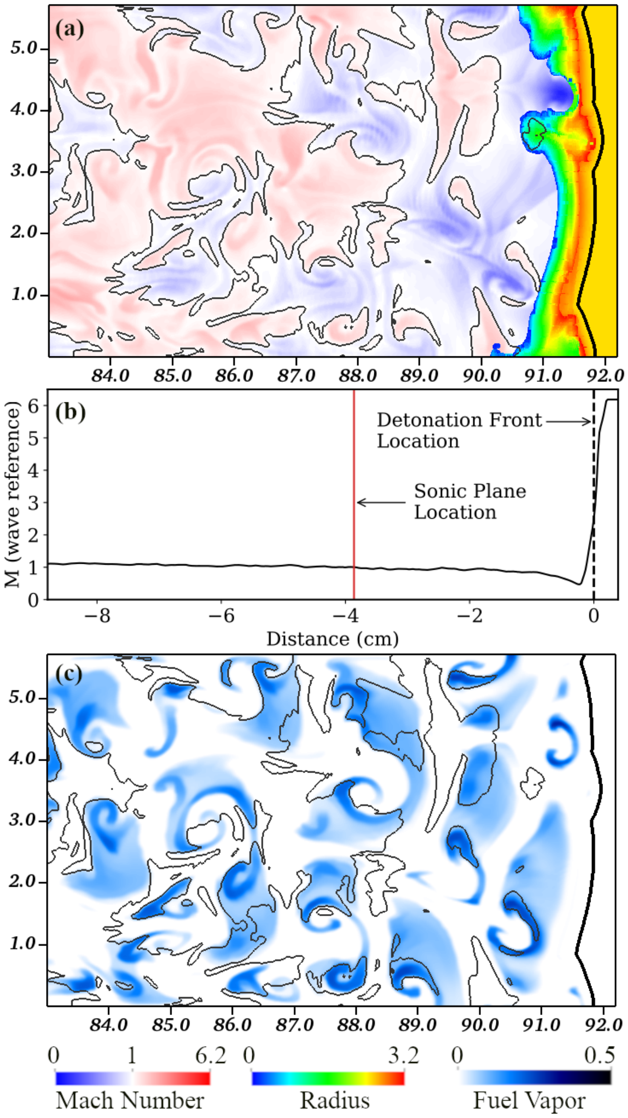

Figure 6: Sonic plane visualization for monodispersed 5 micron droplets without breakup (a) Droplet radius (μm) overlayed on the plot of Mach number in 2D (b) Average Mach number variation behind detonation front (c) Fuel vapor mass fraction.

Though the droplets are initialized uniformly in the pre-shock region, they get redistributed as the detonation wave passes. The curvature of the detonation front and the transverse waves formed by the movement of triple points rearrange the droplets forming low and high particle density regions, which in turn facilitate equivalence ratio (ϕ) variation. Figure 7 displays the particle clustering caused by transverse waves for 10 micron droplets with breakup models. The droplets survive much longer when employing the WERT49 breakup model and show more clustering compared to results from the KHRT model. Figure 8 shows contour plots of equivalence ratio for the 5 μm cases with and without considering breakup. The equivalence ratio is calculated by considering both the amount of liquid and vapor reactants, and those that contributed to the burned products in a computational cell to provide a continuous history

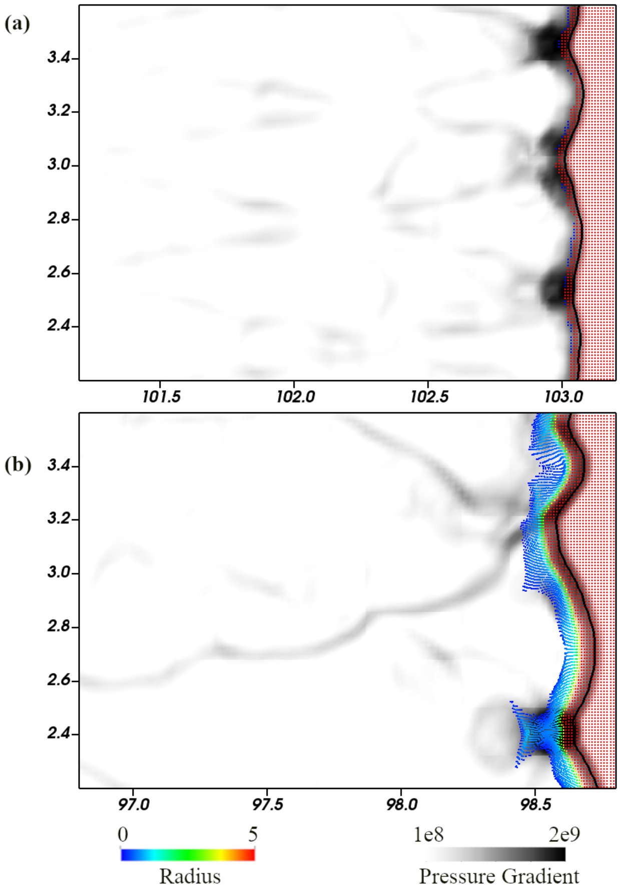

Figure 7: Zoomed in figure showing reorganization of particles for 10 micron monodispersed cases with pressure gradient ($dyne/cm^3$) and particle radius (μm) for the KHRT (a) and the WERT49 (b) breakup models.

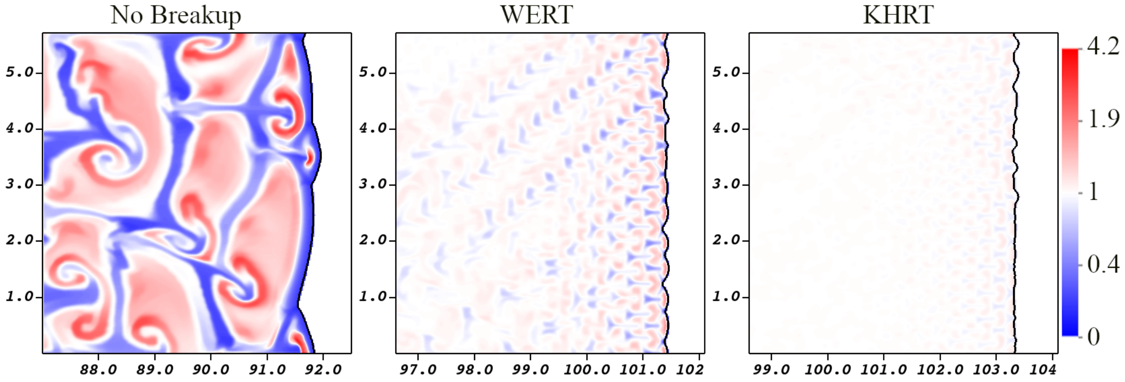

Figure 8: Equivalence ratio behind the detonation wave for 5 μm monodispersed case at 450 μs

in the domain. This equivalence ratio non-uniformity is maximum directly behind the wavefront and, as evaporation rates and gaseous mixing (fuel vapor and oxygen) increase, the distribution of ϕ becomes more uniform. Deviation of ϕ from the global value of one will reduce the available energy that can be contributed to the detonation wave.

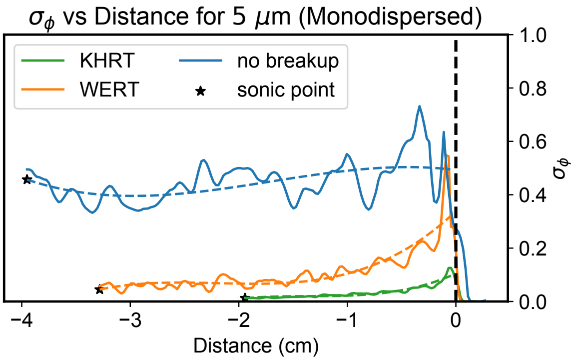

Figure 9: Equivalence ratio variation in transverse direction behind detonation wavefront for 5 micron droplets.The black vertical dotted line is the detonation front location and colored dotted lines represent the time average for respective cases.

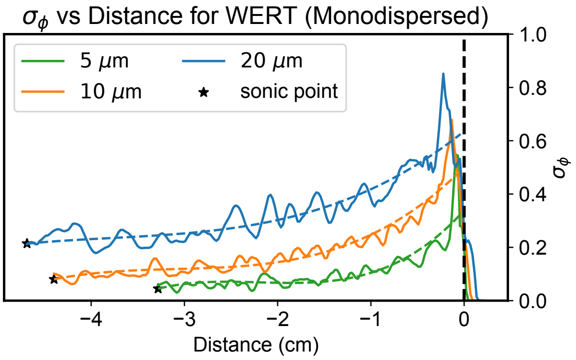

Figure 10: Equivalence ratio variation behind detonation wave for different sizes with WERT49 breakup model. The black vertical dotted line is the detonation front location and colored dotted lines represent the time average for respective cases.

The equivalence ratio is close to unity for most of the regions in the case of KHRT breakup, while more significant deviations from ϕ =1 are seen in the cases of WERT49 breakup and no breakup.

Gaseous mixing occurs due to transverse shock acceleration and shear driving Richtmyer-Meshkov (impulsive acceleration limit of Rayleigh-Taylor instability for compressible fluids [65]) and Kelvin Helmholtz mixing. This mixing of fuel vapor and oxygen is responsible for the decrease in the deviations of ϕ with distance behind the wave. It increases the amount of fuel reacted, and thus reduces the D_{CJ} deficit. Figures 9 and 10 show the standard deviation of ϕ (σ_ϕ) across the y-direction for different breakup models (5 μm droplet cases) and droplet sizes (WERT49 breakup cases). The larger the initial non-uniformity, and the more significant the redistribution of droplets, requiring a longer time for mixing to occur, the higher the observed wave deficit. The two extremes available for inspection are the cases without breakup and those utilizing the KHRT breakup model. In the case of no breakup, there are significantly less transverse waves and much longer mass transfer times, reducing the gas mixing rate and allowing more time for droplet clustering. The KHRT model provides faster mass transfer, and therefore a shorter reaction zone, thus, a smaller cellular structure increasing the amount of transverse waves. The behavior observed in the case of the KHRT model allows for detonation properties much more similar to the gaseous case.

As previously discussed in Section 1.1, initial conditions consisting of spatially non-uniform equivalence ratios are known to produce wave speed deficits in both gaseous experiments and simulations. In multiphase detonations, the initial conditions do not necessarily need to be perturbed to produce spatially non-uniform equivalence ratios since the natural movement of droplets will create variable fuel concentrations. The fuel-oxidizer mixture is always susceptible to developing non-uniform fuel concentrations, and faster breakup times will help minimize this phenomena.

4.3. Polydispersed Particles

For polydispersed particles, simulations without breakup were not run and only results with breakup models are presented in Table 8. The polydispersed cases show larger D_{CJ} deficits than their corresponding monodispersed cases, see Figure 12.

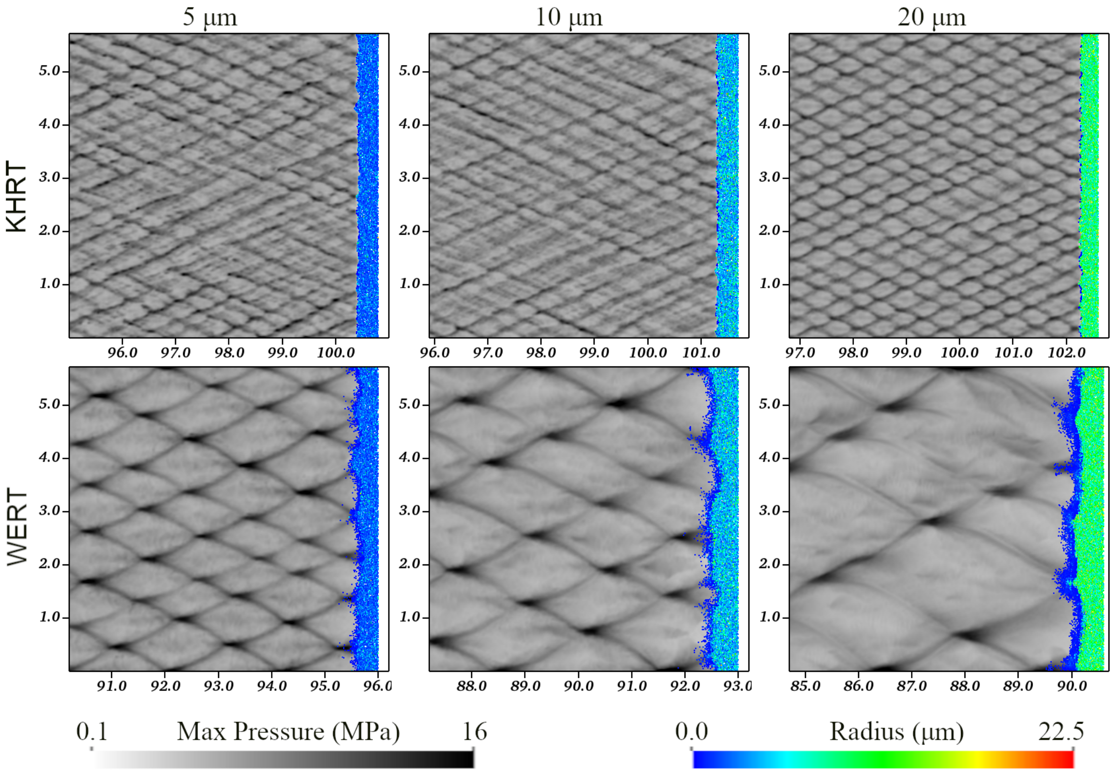

Figure 11: Maximum pressure profiles showing detonation cells for polydispersed particles with breakup at 450 μs

For the simulations run with the KHRT model, the detonation wave for small size distribution ($D_{10} = 5\ \mu m$) is the slowest and for large size distribution ($D_{10} = 20\ \mu m$) is the fastest. This seemingly inconsistent behaviour is the result of using different standard deviations in the particle size distributions. As seen in Figure 13, the initial equivalence ratio distributions in the domain become more centered around one as mean droplet size increases. Pulling from the

Table 8
2D Detonation Results for Polydispersed Particles

Breakup Model	D_{10} μm	Speed (m/s)	ϵ_{gas} (%)	Cell Size (mm)
WERT49	5 μm	2195.6	-7.34	8.16
	10 μm	2106.6	-11.09	12.7
	20 μm	2074.8	-12.44	19.05
KHRT	5 μm	2255.1	-4.83	–
	10 μm	2272.3	-4.11	–
	20 μm	2295.4	-3.13	4.08

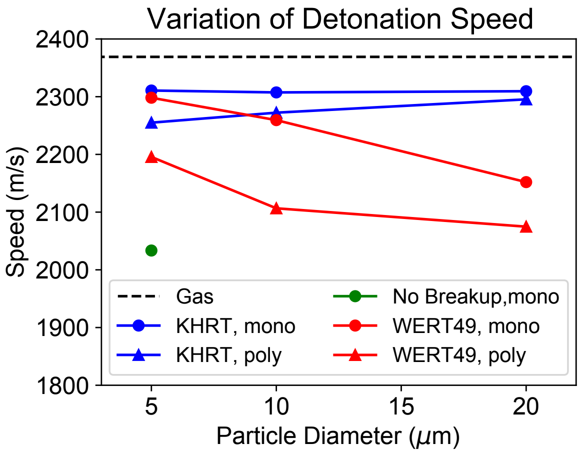

Figure 12: Detonation speed for all multiphase case

Table 9
Sonic length and Parameters at Sonic Plane for Polydispersed Particles

Breakup Model	D_{10}	x_{ds} (cm)	$Y_{p,avg}$	σ_{ϕ}
WERT49	5	4.8	0.945	0.14
	10	5.8	0.937	0.19
	20	5.6	0.85	0.33
KHRT	5	3.57	0.97	0.08
	10	2.92	0.975	0.06
	20	2.43	0.985	0.032

discussion in section 4.2, recall that the average wave speed for the KHRT breakup model is insensitive to the droplet sizes studied in this paper. Thus, it would seem that the observed deficits can be attributed to ϕ non-uniformity, and more specifically, the initial distribution in the domain. Quick evaporation times do not allow for droplet redistribution so the equivalence ratio distribution in the post-shock region is roughly the same in the pre-shock. From Figure 13, we can see that the initial degree of non-uniformity is proportional to the standard deviation of the lognormal distribution

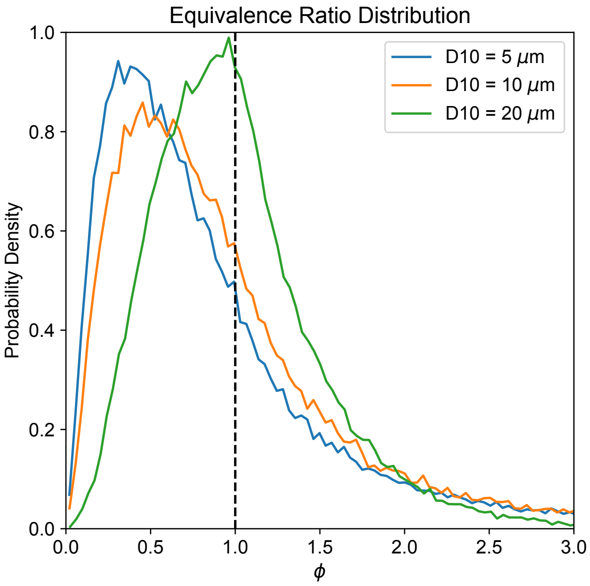

Figure 13: Initial ϕ distribution in the domain due to polydispersity for three cases

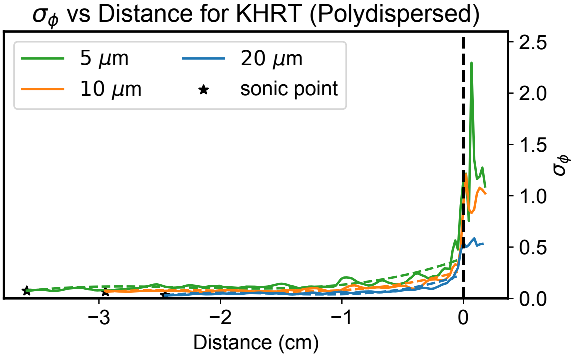

Figure 14: Equivalence ratio variation behind detonation wave for different distributions with KHRT breakup model.The black vertical dotted line is the detonation front location and colored dotted lines represent the time average for respective cases.

of droplets, giving largest non-uniformity of ϕ for small size distribution. Consequently, the speed for this distribution is the lowest among three.

The simulations utilizing the WERT49 breakup model show different behavior where with increasing D_{10}, the wave speed decreases similar to that in the monodispersed cases. The strong dependence of droplet breakup time with size leaves enough time for particle reorganization and vapor mixing behind the wave, thus changing the initial distribution of equivalence ratio. Even though large size distribution is more uniform initially, the lifetime of larger droplets extend the times for redistribution and, with less transverse waves, decrease effective vapor mixing.

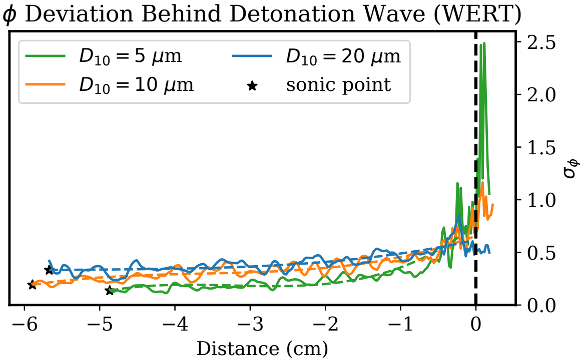

Figure 15: Equivalence ratio variation behind detonation wave for different distributions with WERT49 breakup model.The black vertical dotted line is the detonation front location and colored dotted lines represent the time average for respective cases.

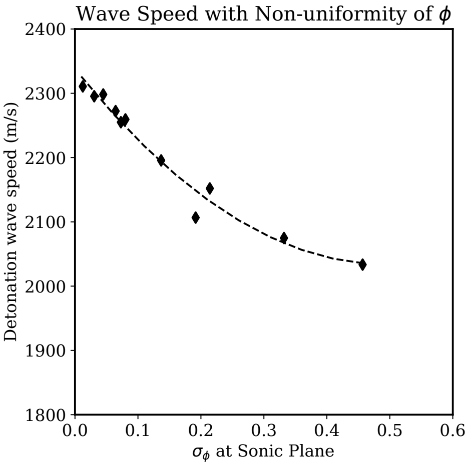

Figure 16: Variation of Detonation speed with the equivalence ratio non-uniformity at the sonic point.

Similar to what was observed in the monodispersed cases, the trend of σ_ϕ at the sonic plane and wave deficit appears to hold true for the polydispersed cases. Figures 14 and 15 show consistent trends which explain the somewhat non-intuitive results of the KHRT model. The value of σ_ϕ at the sonic plane has the largest effect on the detonation velocity, though the value of σ_ϕ at the pre-shock conditions must also be considered as it is the basis for σ_ϕ at the sonic plane. Figure 16 plots average detonation speed verses σ_ϕ at the sonic plane for all of the cases run , and shows a strong correlation between detonation speed and σ_ϕ at the sonic plane.

4.4. Comparison to Known Experiments

While we are unable to directly compare to existing experiments, there exist a few relevant experiments that we can compare to. Gaseous oxygen detonations utilizing decane have a CJ state similar to the dodecane system, i.e. $D_{CJ} = 2337.85$ m/s, $P_{CJ} = 4.09$ MPa, $T_{CJ} = 3867.04$ K, and $\rho_{CJ} = 2.94$ kg/m^3 as predicted by the SDToolbox via the JetSurF2.0 mechanism. Additionally, both liquids are low vapor pressure, heavy hydrocarbon fuels with similar thermophysical properties. Tang et al. [87] reported detonation wave velocities for their experiments where deficits are roughly 20% compared to the theoretical gaseous D_{CJ} across a range of lean equivalence ratios for droplet diameters of 400 μm. Comparing to the present study, extrapolation of the speed deficit trend predicted by the WERT49 model may be in line with such experimental results, considering the large size of these droplets.

Papavassiliou et al. [69] provide detonation wave speeds and cell sizes for a range of equivalence ratios and nitrogen dilution for decane-oxygen detonations. For an equivalence ratio near unity and no nitrogen dilution, cell sizes are reported to be 4 mm and D_{CJ} deficits in a 10 μm fog are approximated to be 2.5%. The results of the KHRT model reasonably agree with the work of Papavassiliou et al. since the cell sizes are measured on average to be 4.76 mm with a wave velocity deficit of 2.6%.

Other work from Lu et al. [56] can help us interpret the qualitative trends we see in our results, specifically, looking at the relationships between different droplet sizes and their effect on the dynamic wave front. Their work presents detonations in sprays of fogs ($< \varnothing 10\mu$m), 700 μm, and 1400 μm heptane droplets. With increasing droplet size, there is a decrease in transverse wave frequency resulting in larger cellular structures. While the droplet variation of that study is much more significant than what is presented in this work, this trend is still observed in our polydispersed simulations where increasing the mean diameter yielded more coherent (KHRT model) and larger (WERT49 model) cells in polydispersed simulations.

5. Conclusions

The current study simulated gas-liquid hydrocarbon detonation utilizing an Euler-Lagrange (EL) numerical framework with accurate thermodynamic accounting and a global kinetic mechanism. Detonation-driven breakup mechanisms have yet to be explored in detail in experiments, thus two previous droplet breakup models were investigated, one an empirical correlation based on shock-tube experiments and another a widely used semi-theoretical model based on the growth of hydrodynamic instabilities. The inclusion of droplet breakup models yielded detonation behavior that is more consistent with previous experimental observations. The absence of a breakup model yielded unsteady or failed detonation waves in sprays of 10 and 20 μm diameter droplets where detonations are known to occur in previous experiments. While the inclusion of a breakup model is deemed necessary, there are still significant differences in the results depending on the type of model and implementation, warranting further investigation of breakup model parameters. For the cases considered here utilizing small droplet sizes ($< \varnothing 45\mu$m), the best results for recovering D_{CJ} and cell sizes similar to the experimental observations of Papavassiliou et al. [69] are believed to be obtained from the semi-theoretical model utilizing Kelvin-Helmholtz/Rayleigh-Taylor instability theory. On the other hand, the trend of increasing D_{CJ} deficits with increasing droplet size, observed in other experimental and simulation works, was best captured by the empirical (WERT49) model derived from shock tube experimental data.

Possible explanations for the observed velocity deficits were explored. The three largest contributors to wave speed deficits (in order of importance) are believed to be: 1) redistribution of droplets by post-detonation 2D gas hydrodynamics, 2) energy losses (latent heat of vaporization) required for phase change, and 3) pre-detonation spatial perturbations in equivalence ratio inherent to natural droplet spatial and size distributions. Contributors one and three result in fuel vapor escaping past the sonic point (with respect to detonation wave), thus reducing the reaction energy available for wave propagation. The major conclusions of the study are outlined below.

- Droplets falling behind the sonic plane are unlikely to be the source of detonation speed deficits observed in multiphase detonations of small droplets ($< \varnothing 45$). Overall, larger reaction zone lengths are observed in multiphase detonations, allowing more time for multiphase hydrodynamic mixing and droplet reaction.
- Multiphase detonations will concentrate fuel behind the wave front due to multiphase hydrodynamic redistribution of droplets. This redistribution will enhance non-uniformity in the equivalence ratio leading to pockets of fuel that cannot completely react before passing the sonic plane. This loss of reaction energy is the largest contributor to detonation velocity deficits.
- The breakup process will determine the lifetime of droplets in the post-detonation conditions. Droplets that survive longer will have more time to be redistributed, resulting in greater inhomogeneity of equivalence ratios.
- The breakup process will determine the overall reaction process rate. Faster breakup processes will result in faster reaction and smaller detonation cells and more frequent transverse waves.
- Gas hydrodynamic mixing acts to make the equivalence ratio more uniform. Stronger and more frequent transverse waves act to increase this gas mixing and reduce detonation velocity deficits.

Realistic detonation conditions are going to demand the modeling of polydisperse sprays with droplets ranging from submicron to millimeter. Current particle-in-cell methods are lacking in accuracy when interpolating properties between the Eulerian mesh and Lagrangian points when the smallest discrete fluid element and point to be modeled have a length ratio of less than 5-10. Given the necessary resolution to capture the shock dynamics of a detonation wave front, this presents a problem from a modeling standpoint. Methods will need to evolve to accommodate both needs to obtain the best simulation results.

The breakup process in a multiphase detonation is relatively unexplored, yet it has possibly the greatest overall effect on multiphase detonation properties. Hydrodynamic breakup mechanisms likely play a significant role in detonation-driven breakup, but this must be confirmed in future work and other possible mechanisms (e.g. cavitation) considered.

The experimental measurement of multiphase detonation processes is challenging. More studies on the fundamental physics of the liquid hydrocarbon detonation problem (droplet breakup in particular) are needed to fully characterize the observed behavior presented in literature. Quantification of metrics such as detonation speeds and cell sizes, over a wide range of initial conditions (droplet sizes, equivalence ratios, pressure and temperatures) will boost the overall confidence in multiphase simulation methods.

6. Acknowledgements

This work was supported by the National Science Foundation through award numbers 1933479 and 2044767 and the Office of Naval Research through contract number N00014-20-1-2796. The computation for this work was performed in part on the high performance computing infrastructure provided by Research Support Solutions and in part by the National Science Foundation under grant number CNS-1429294 at the University of Missouri, Columbia MO. Portions of this research were conducted with the advanced computing resources provided by Texas A&M High Performance Research Computing.

CRediT authorship contribution statement

Benjamin J. Musick: Draft preparation, code development, research. **Manoj Paudel:** Draft preparation, code development, research, model selection/analysis, data post-processing. **Praveen K. Ramaprabhu:** In depth consultation and advisement. **Jacob A. McFarland:** Principal investigator.

References

[1] B. Abramzon and W. Sirignano. Droplet vaporization model for spray combustion calculations. *Int. J. Heat Mass Tran.*, 32:1605–1618, 1989.

[2] M. J. Andrews and P. J. O'rourke. The multiphase particle-in-cell (mp-pic) method for dense particulate flows. *Int. J. Multiphas. Flow*, 22:379–402, 1996.

[3] J. C. Beale and R. D. Reitz. Modeling spray atomization with the kelvin-helmholtz/rayleigh-taylor hybrid model. *Atomization Spray*, 9(6):623–650, 1999.

[4] M. A. Benmahammed, B. Veyssiere, B. A. Khasainov, and M. Mar. Effect of gaseous oxidizer composition on the detonability of isooctane–air sprays. *Combust. Flame*, 165:198–207, 2016.

[5] M. E.-A. Benmahammed. *Détonations dans les aérosols de gouttelettes liquides réactives. Etude de l'influence des propriétés physicochimiques de la phase liquide et de l'oxydant gazeux.* PhD thesis, Poitiers, France, 2013.

[6] L. Boeck, F. Berger, J. Hasslberger, and T. Sattelmayer. Detonation propagation in hydrogen–air mixtures with transverse concentration gradients. *Shock Waves*, 26(2):181–192, 2016.

[7] V. M. Boiko, A. N. Papyrin, and S. V. Poplavskii. Dynamics of droplet breakup in shock waves. *J. Appl. Mech. Tech. Phy.*, 28(2):263–269, 1987.

[8] J. Bowen, K. Ragland, F. Steffes, and T. Loflin. Heterogeneous detonation supported by fuel fogs or films. *Symp. (Int.) Combust.*, 13(1):1131–1139, 1971.

[9] B. Boyd and D. Jarrahbashi. Numerical study of the transcritical shock-droplet interaction. *Phys. Rev. Fluids*, 6(11):113601, 2021.

[10] S. M. Briggs, N. Berube, D. R. Dyson, R. Forehand, M. P. Kinzel, S. Vasu, S. Grace, and P. Anderson. Experiments on water droplet breakup in a detonation medium. In *AIAA SCITECH 2023 Forum*, page 2257, 2023.

[11] D. C. Bull, M. A. McLeod, and G. A. Mizner. *Detonation of Unconfined Fuel Aerosols*, pages 48–60. 1979.

[12] A. Burcat and S. Eidelman. Evolution of a detonation wave in a cloud of fuel droplets: Part ii. influence of fuel drops. *AIAA J.*, 18:1233–1236, 1980.

[13] X.-K. Cao, Z.-G. Sun, W.-F. Li, H.-F. Liu, and Z.-H. Yu. A new breakup regime of liquid drops identified in a continuous and uniform air jet flow. *Phys. Fluids.*, 19(5):057103, 2007.

[14] J. Char, W. Liou, and J. Yeh. Ignition and combustion study of jp-8 fuel in a supersonic flowfield. *Shock Waves*, 6:259–266, 1996.

[15] S. Cheatham and K. Kailasanath. Numerical modelling of liquid-fuelled detonations in tubes. *Combust. Theor. Model*, 9(1):23–48, 2005.

[16] W.-H. Chou and G. Faeth. Temporal properties of secondary drop breakup in the bag breakup regime. *Int. J. Multiphas. Flow*, 24(6):889–912, 1998.

[17] R. Clift, J. R. Grace, and M. E. Weber. Bubbles, drops, and particles. 1978.

[18] P. Colella and P. R. Woodward. The piecewise parabolic method (ppm) for gas-dynamical simulations. *J. Comput. Phys.*, 54(1):174–201, 1984.

[19] F. B. Cramer. The onset of detonation in a droplet combustion field. *Symp. (Int.) Combust.*, 9(1):482–487, 1963.

[20] C. Crowe, J. Schwarzkopf, M. Sommerfeld, and Y. Tsuji. *Multiphase Flows with Droplets and Particles*. CRC Press, 2011.

[21] E. Dabora, K. Ragland, and J. Nicholls. Drop-size effects in spray detonations. *Symp. (Int.) Combust.*, 12(1):19–26, 1969.

[22] J. Dahal and J. A. McFarland. A numerical method for shock driven multiphase flow with evaporating particles. *J. Comput. Phys.*, 344:210–233, 2017.

[23] Z. Dai and G. Faeth. Temporal properties of secondary drop breakup in the multimode breakup regime. *Int. J. Multiphas. Flow*, 27(2):217–236, 2001.

[24] V. Duke-Walker, W. C. Maxon, S. R. Almuhna, and J. A. McFarland. Evaporation and breakup effects in the shock-driven multiphase instability. *J. Fluid Mech.*, 908:A13, 2021.

[25] V. Duke-Walker, B. J. Musick, and J. A. McFarland. Experiments on the breakup and evaporation of small droplets at high weber number. *Int. J. Multiphas. Flow*, 161:104389, 2023.

[26] A. Dworzanczyk, N. J. Parziale, C. Croft, D. Wise, and M. Libeau. High-speed imaging of interaction of liquid drops with hypersonic projectiles. In *AIAA AVIATION 2023 Forum*, page 4248, 2023.

[27] D. Dyson, S. Vasu, A. Arakelyan, N. Berube, S. Briggs, J. Ramirez, E. M. Ninnemann, K. Thurmond, G. Kim, W. H. Green, et al. Detonation wave-induced breakup and combustion of rp-2 fuel droplets. In *AIAA SCITECH 2022 Forum*, page 1453, 2022.

[28] W. Döring. Über detonationsvorgang in gasen. *Ann. Phys.*, 43:421–436, 1943.

[29] S. Eidelman and A. Burcat. Evolution of a detonation wave in a cloud of fuel droplets: Part i. influence of igniting explosion. *AIAA J.*, 18:1103–1108, 1980.

[30] S. Eidelman and A. Burcat. The mechanism of a detonation wave enhancement in a two-phase combustible medium. *Symp. (Int.) Combust.*, 18(1):1661–1670, 1981. Eighteenth Symp Combust Proc.

[31] W. Fickett and W. C. Davis. Detonation: theory and experiment. 2000.

[32] S. Frolov. Initiation of heterogeneous detonation in tubes with coils and shchelkin spiral. *High Temp+*, 44(2):283–290, 2006.

[33] S. Frolov and B. Gel'fand. On the limiting diameter for propagation of gas detonation in tubes. *Doklady USSR Acad. Sci.*, 312(5):1177–1180, 1990.

[34] Frolov, S. M. Detonation initiation techniques for pulse detonation propulsion, 2009.

[35] B. Fryxell, K. Olson, P. Ricker, F. X. Timmes, M. Zingale, D. Q. Lamb, P. MacNeice, R. Rosner, J. W. Truran, and H. Tufo. FLASH: An adaptive mesh hydrodynamics code for modeling astrophysical thermonuclear flashes. *The Astrophysical Journal Supplement Series*, 131(1):273–334, nov 2000.

[36] A. Gavrikov, A. Efimenko, and S. Dorofeev. A model for detonation cell size prediction from chemical kinetics. *Combust. Flame*, 120(1):19–33, 2000.

[37] G. Godsave. Studies of the combustion of drops in a fuel spray—the burning of single drops of fuel. *Symp. (Int.) Combust.*, 4(1):818–830, 1953. Fourth Symp Combust Proc.

[38] D. G. Goodwin, H. K. Moffat, and R. L. Speth. Cantera: An object-oriented software toolkit for chemical kinetics, thermodynamics, and transport processes. `http://www.cantera.org`, 2017. Version 2.3.0.

[39] A. K. Hayashi, N. Tsuboi, and E. Dzieminska. Numerical study on jp-10/air detonation and rotating detonation engine. *AIAA J.*, 58(12):5078–5094, 2020.

[40] D. C. Horning. *A Study of the High-Temperature Autoignition and Thermal Decomposition of Hydrocarbons*. PhD thesis, Stanford, California 94305-3032, 2001.

[41] L.-P. Hsiang and G. Faeth. Near-limit drop deformation and secondary breakup. *Int. J. Multiphas. Flow*, 18(5):635–652, 1992.

[42] Z. Huang, M. Zhao, Y. Xu, G. Li, and H. Zhang. Eulerian-lagrangian modelling of detonative combustion in two-phase gas-droplet mixtures with openfoam: Validations and verifications. *Fuel*, 286:119402, 2021.

[43] M. Jalaal and K. Mehravaran. Transient growth of droplet instabilities in a stream. *Phys. Fluids.*, 26(1):012101, 2014.

[44] E. Jouguet. Sur la propagation des réactions chimiques dans les gaz [on the propagation of chemical reactions in gases]. *J. Math Pure Appl.*, 6(1):347–425, 1905.

[45] E. Jouguet. Sur la propagation des réactions chimiques dans les gaz [on the propagation of chemical reactions in gases]. *J. Math Pure Appl.*, 6(2):5–85, 1906.

[46] H. Jääskeläinen and M. K. Khair. Combustion in diesel engines. `https://dieselnet.com/tech/diesel_combustion.php`, 2020.

[47] K. Kailasanath. Liquid-fueled detonations in tubes. *J. Propul. Power*, 22(6):1261–1268, 2006.

[48] K. Kailasanath. *Recent Developments in the Research on Pressure-Gain Combustion Devices*, pages 3–21. Springer Singapore, Singapore, 2020.

[49] D. Kessler, V. Gamezo, and E. Oran. Gas-phase detonation propagation in mixture composition gradients. *Philos T R Soc A*, 370(1960):567–596, 2012.

[50] J. Kindracki. Study of detonation initiation in kerosene–oxidizer mixtures in short tubes. *Shock Waves*, 24:603–618, 2014.

[51] Y. Kozak, D. Sai Sandeep, and A. Poludnenko. Design and construction of a liquid-fuel detonation tube facility. In *APS Division of Fluid Dynamics (Fall)*, 2020.

[52] E. D. Laboratory. Shock and detonation toolbox. `https://shepherd.caltech.edu/EDL/PublicResources/sdt/`, 2021.

[53] J. H. S. Lee. *The Detonation Phenomenon*. Cambridge University Press, 2008.

[54] A. Liu, D. Mather, and R. Reitz. Modeling the effects of drop drag and breakup on fuel sprays. *SAE Tech. Paper 930072*, page 17, 03 1993.

[55] X.-Y. Liu, M.-Y. Luan, Y.-L. Chen, and J.-P. Wang. Propagation behavior of rotating detonation waves with premixed kerosene/air mixtures. *Fuel*, 294:120253, 2021.

[56] P. Lu, N. Slagg, B. Fishburn, and P. Ostrowski. Relation of chemical and physical processes in two-phase detonations. *Acta. Astronaut.*, 6(7):815–826, 1979.

[57] T. Lu and C. K. Law. Heterogeneous effects in the propagation and quenching of spray detonations. *J. Propul. Power*, 20(5):820–827, 2004.

[58] K. Luo, O. Desjardins, and H. Pitsch. Dns of droplet evaporation and combustion in a swirling combustor. *Center for Turbulence Research, Annual Research Briefs*, pages 253–265, 2008.

[59] P. MacNeice, K. M. Olson, C. Mobarry, R. deFainchtein, and C. Packer. Paramesh: A parallel adaptive mesh refinement community toolkit. Technical report, NASA, Greenbelt, Maryland 20771, 1999.

[60] M. Mar. *Détonations dans les aérosols de gouttelettes de carburants liquides: Étude de l'influence de la granulométrie des gouttelettes*. PhD thesis, Poitiers, France, 2013.

[61] J. A. McFarland, W. J. Black, J. Dahal, and B. E. Morgan. Computational study of the shock driven instability of a multiphase particle-gas system. *Phys. Fluids.*, 28(2):024105 1–32, Feb. 2016.

[62] J. C. Meng and T. Colonius. Numerical simulation of the aerobreakup of a water droplet. *J. Fluid Mech.*, 835:1108–1135, 2018.

[63] Q. Meng, M. Zhao, H. Zheng, and H. Zhang. Eulerian-lagrangian modelling of rotating detonative combustion in partially pre-vaporized n-heptane sprays with hydrogen addition. *Fuel*, 290:119808, 2021.

[64] Q. Meng, N. Zhao, and H. Zhang. On the distributions of fuel droplets and in situ vapor in rotating detonation combustion with prevaporized n-heptane sprays. *Phys. Fluids.*, 33:043307, 2021.

[65] M. Mohaghar, J. McFarland, and D. Ranjan. Three-dimensional simulations of reshocked inclined richtmyer-meshkov instability: Effects of initial perturbations. *Phys. Rev. Fluids*, 7(9):093902, 2022.

[66] J. A. NICHOLLS and A. A. RANGER. Aerodynamic shattering of liquid drops. *AIAA J.*, 7(2):285–290, 1969.

[67] P. J. O'rourke and A. A. Amsden. The tab method for numerical calculation of spray droplet breakup. 1987.

[68] D. L. C. B. (Oxon.). Vi. on the rate of explosion in gases. *Lond. Edinb. Dublin Philos. Mag.*, 47(284):90–104, 1899.

[69] J. Papavassiliou, A. Makris, R. Knystautas, J. H. Lee, C. K. Westbrook, and W. J. Pitz. *Measurements of Cellular Structure in Spray Detonation*, pages 148–169. 1991.

[70] F. Petitpas, R. Saurel, and Franquet. Modelling detonation waves in condensed energetic materials: multiphase cj conditions and multidimensional computations. *Shock Waves*, 19:377–401, 2009.

[71] M. Pilch and C. Erdman. Use of breakup time data and velocity history data to predict the maximum size of stable fragments for acceleration-induced breakup of a liquid drop. *Int. J. Multiphas. Flow*, 13:741–757, 1987.

[72] F. Pintgen and J. Shepherd. Simultaneous soot foil and plif imaging of propagating detonations. In *19th ICDERS*, 2003.

[73] B. E. Poling, J. M. Prausnitz, and J. P. O'connell. *Properties of gases and liquids*. McGraw-Hill Education, 2001.

[74] K. Ragland, E. Dabora, and J. Nicholls. Observed structure of spray detonations. *The Phys. Fluids.*, 11(11):2377–2388, 1968.

[75] W. Ranz and W. Marshall. Evaporation from drops. *Chem. Eng. Prog.*, 48(3):141–146, 1952.

[76] R. Reitz et al. Modeling atomization processes in high-pressure vaporizing sprays. *Atomization Spray Technol.*, 3(4):309–337, 1987.

[77] G. Roy, S. Frolov, A. Borisov, and D. Netzer. Pulse detonation propulsion: challenges, current status, and future perspective. *Prog. Energ. Combust.*, 30(6):545–672, 2004.

[78] M. Samirant. *Dispersion-Initiation and Detonation of Liquid and Dust Aerosols-Experiences Derived from Military Fuel-Air Explosives*, pages 123–134. Springer Netherlands, Dordrecht, 1999.

[79] E. Schultz and J. Shepherd. Validation of detailed reaction mechanisms for detonation simulation. 2000.

[80] D. A. Schwer. *Multi-dimensional Simulations of Liquid-Fueled JP10/Oxygen Detonations*, pages 1–18.

[81] D. A. Schwer, J. Eugene P. O'Fallon, and D. A. Kessler. Liquid-fueled detonation modeling at the u.s. naval research laboratory. Technical report, Naval Research Laboratory, Washington, DC 20375-5320, 2018.

[82] S. Sembian, M. Liverts, N. Tillmark, and N. Apazidis. Plane shock wave interaction with a cylindrical water column. *Physics of Fluids*, 28(5), 2016.

[83] H. Shen, G. Wang, K. Liu, and D. Zhang. Numerical simulation of liquid-fueled detonations by an eulerian–lagrangian model. *Int. J. Nonlin. Sci. Num.*, 13(2):177–188, 2012.

[84] D. M. Snider, S. M. Clark, and P. J. O'Rourke. Eulerian–lagrangian method for three-dimensional thermal reacting flow with application to coal gasifiers. *Chem. Eng. Sci.*, 66(6):1285–1295, 2011.

[85] D. Spalding. A standard formulation of the steady convective mass transfer problem. *Int. J. Heat Mass Tran.*, 1(2-3):192–207, Aug. 1960.

[86] T. Su, M. Patterson, R. D. Reitz, and P. Farrell. Experimental and numerical studies of high pressure multiple injection sprays. *SAE Trans.*, pages 1281–1292, 1996.

[87] M. Tang, J. Nicholls, M. Sichel, and Z. Lin. The direct initiation of detonation in decane-air and decane-oxygen sprays. Technical report, Ann Arbor, Michigan, 1983.

[88] T. Theofanous. Aerobreakup of newtonian and viscoelastic liquids. *Annu. Rev. Fluid Mech.*, 43(1):661–690, 2011.

[89] T. Theofanous and G. Li. On the physics of aerobreakup. *Phys. Fluids.*, 20:052103, 05 2008.

[90] B. Veyssiere, B. Khasainov, M. Mar, and M. Benmahammed. Investigation of detonation propagation regimes in liquid sprays. In *24th ICDERS*, 2013.

[91] J. von Neumann. *Theory of detonation waves. Progress Report to the National Defense Research Committee Div. B*, page 178–218. OSRD-549 (PB 31090). New York: Pergamon Press, 1942.

[92] D. Voronin and S. Zhdan. Calculation of heterogeneous detonation initiation for a hydrogen-oxygen mixture in an explosion tube. *Combust. Explo. Shock*+, 20(4):461–465, 1984.

[93] H. Wang, E. Dames, B. Sirjean, D. A. Sheen, R. Tango, A. Violi, J. Y. W. Lai, F. N. Egolfopoulos, D. F. Davidson, R. K. Hanson, C. T. Bowman, C. K. Law, W. Tsang, N. P. Cernansky, D. L. Miller, and R. P. Lindstedt. A high-temperature chemical kinetic model of n-alkane (up to n-dodecane), cyclohexane, and methyl-, ethyl-, n-propyl and n-butyl-cyclohexane oxidation at high temp+s, jetsurf version 2.0. `http://web.stanford.edu/group/haiwanglab/JetSurF/JetSurF2.0/index.html`, 2010.

[94] Y. Wang, Z. Chen, and H. Chen. Propagation of gaseous detonation in spatially inhomogeneous mixtures. *Phys. Fluids.*, 33(11):116105, 2021.

[95] W. T. Webber. Spray combustion in the presence of a travelling wave. *Symp. (Int.) Combust.*, 8(1):1129–1140, 1961. Eighth Symp Combust Proc.

[96] K. Wert. A rationally-based correlation of mean fragment size for drop secondary breakup. *Int. J. Multiphas. Flow*, 21(6):1063–1071, 1995.

[97] C. K. Westbrook and F. L. Dryer. Simplified reaction mechanisms for the oxidation of hydrocarbon fuels in flames. *Combust. Sci. Technol.*, 27(1-2):31–43, 1981.

[98] C. Young, J. McFarland, and P. Ramaprabhu. Design and construction of a liquid-fuel detonation tube facility. In *APS Division of Fluid Dynamics (Fall)*, 2020.

[99] Y. Zel'dovich. On the theory of the propagation of detonations on gaseous system. *J. Exp. Theor. Phys*+, 10:542–568, 1940.

[100] M. Zhao and H. Zhang. Numerical simulation of two-dimensional detonation propagation in partially pre-vaporized n-heptane sprays. *ICLASS Edinburgh: Fuel Sprays & Combustion*, 1:1–8, 2021.

[101] Y. Zhou, X. Zhang, L. Zhong, R. Deiterding, L. Zhou, and H. Wei. Effects of fluctuations in concentration on detonation propagation. *Phys. Fluids.*, 34(7):076101, 2022.

A. Appendix

The appendix contains more detailed information on our numerical methods and models so that the reader may understand our methods in greater detail if desired, and so that our results and methods may be reproduced. The information is presented succinctly with little description, focusing primarily on the equations and algorithms.

A.1. Particle Source and Solution Algorithm

One time marching cycle consists of what can be seen in Algorithm 1, where Δt is the cycle time step used by the gas calculations, n_s is the number of particle substeps per gas time step, and Δt_p the particle time substep.

Algorithm 1 **Gas-Particle Coupling and Reaction**

```
STEP 1: Solve conservation equations without source
  → calculate fluxes using Riemann solver
  → update gas properties using fluxes
STEP 2: Calculate particle source terms and update gas
  for each substep $\Delta t_p = \Delta t/n$ do
    for each particle do
      → Calculate drag (Appendix A.5 and Alg 5 for WERT49 breakup model )
      → Calculate evaporation (Alg 2)
      → Update particle properties and location
      → calculate particle source terms
    end for
    → Map source terms to gas mesh
    → Update gas properties with particle source terms
  end for
STEP 3: Carry out particle breakup calculations (Alg 3 or 4)
STEP 4: Carry out Reaction Calculation and Update
```

Equations 27 - 29 give the source terms per unit volume of the gas mesh, $V_{mesh,cell}$. $\mathcal{I}$ represents the interpolation operator and N the total number of particles in the domain.

$$M_p = \frac{1}{V_{mesh,cell}} \sum_{k=1}^{N} \mathcal{I} \frac{dm_{p,k}}{dt} \tag{27}$$

$$\mathbf{F}_p = \frac{1}{V_{mesh,cell}} \sum_{k=1}^{N} \mathcal{I} \frac{dm_{p,k}\mathbf{v}_{p,k}}{dt} \tag{28}$$

$$E_p = \frac{1}{V_{mesh,cell}} \sum_{k=1}^{N} \mathcal{I} \frac{dm_{p,k}e_{p,k}}{dt} \tag{29}$$

A.2. Heat & Mass Transfer

The process for heat and mass transfer follows that of Abramzon and Sirignano [1]. The algorithm occurs during the "update particle properties" step in algorithm 1 and can be seen in algorithm 2, where B_T is iteratively calculated within the tolerance, $\epsilon = 10^{-2}$.

Algorithm 2 **Heat & Mass Transfer**

```
STEP 1: Find fuel vapor fraction at drop surface
STEP 2: Compute weighted gas phase properties at $\bar{T}$
STEP 3: Update $Re$, $Sh_0$, $Nu_0$, $B_M$, $F_M$, and $Sh^*$
STEP 4: Carry out mass transfer calculation, $\dot{m}$
STEP 5: Iterate for $B_T$
    while $|B_T^n - B_T^{n+1}| > \epsilon$ do
        → Find $F_T$ from previous or guessed $B_T$
        → Calculate $Nu^*$ and $\phi$
        → Update $B_T$
    end while
STEP 6: Carry out heat transfer calculation, $Q_L$
```

Molar and mass fuel vapor fractions at the surface of the droplet are found as,

$$x_{f,s} = p_{F,s}/p \tag{30}$$

$$Y_{F,s} = x_{F,s} W_f / \sum_i x_i W_i \tag{31}$$

where saturated pressure is a function of the current droplet temperature, $p_{F,s} = p_{F,s}(T_s)$. Transport properties are calculated at the weighted average film condition: gas viscosity $\bar{\mu}_g$, Lewis number $\bar{Le} = \bar{k}_g/(\bar{\rho}_g \bar{D}_g \bar{C}_{p,g})$, Prandtl number $\bar{Pr} = \bar{C}_{p,g}\bar{\mu}_g/\bar{k}_g$, and Schmidt number $\bar{Sc} = \bar{\mu}_g/(\bar{\rho}_g \bar{D}_g)$. These properties are evaluated at the film temperature and mass fractions shown in equations 32 and 33, where A_r is the film weighting factor taken to be 1/3.

$$\bar{T} = T_s + A_r(T_\infty - T_s); \tag{32}$$

$$\bar{Y}_F = Y_{F,s} + A_r(Y_{F,\infty} - Y_{F,s}) \tag{33}$$

The Reynolds number calculated in Equation 34,

$$Re = \frac{2\rho_\infty |\mathbf{v}_g - \mathbf{v}_p| r_p}{\bar{\mu}_g} \tag{34}$$

Nusselt and Sherwood Numbers are the non-dimensional heat and mass transfer coefficients defined by Equation 35

$$\begin{aligned} Nu &= -\frac{2r_p}{T_s - T_\infty}\left(\frac{dT}{dr}\right)_s \\ Sh &= -\frac{2r_p}{Y_{F,s} - Y_{F,\infty}}\left(\frac{dY_F}{dr}\right)_s \end{aligned} \tag{35}$$

These numbers can be calculated using the Frossling correlations or the correlations suggested by Clift et al. [17]. For our approach, we use the relations offered by Clift et. seen in equations 36 and 37.

$$\begin{aligned} Sh_0 &= 1 + (1 + Re\bar{P}r)^{1/3} f(Re) \\ Nu_0 &= 2 + (1 + Re\bar{S}c)^{1/3} f(Re) \end{aligned} \tag{36}$$

$$f(Re) = \begin{cases} 1 & Re \leq 1 \\ Re^{0.077} & 1 < Re \leq 400 \end{cases} \tag{37}$$

F_M & F_T are correction factors for mass and heat transfer found according to Equation 38, where the subscript x may be T or M for the heat and mass transfer number respectively.

$$F(B_x) = (1 + B_x)^{0.7} \frac{\ln(1 + B_x)}{B_x} \tag{38}$$

The modified Sherwood and Nusselt numbers can be computed according to Equation 39.

$$\begin{aligned} Sh^* &= 2 + (Sh_0 - 2)/F_M \\ Nu^* &= 2 + (Nu_0 - 2)/F_T \end{aligned} \tag{39}$$

The Spalding number may then be calculated as shown in equation 40, where ψ is found using Equation 41,

$$B_T = (1 + B_M)^{\psi} - 1 \tag{40}$$

$$\psi = \frac{\bar{C}_{p,F}}{\bar{C}_{p,g}} \frac{Sh^*}{Nu^*} \frac{1}{\bar{Le}} \tag{41}$$

Heat absorbed by the liquid droplet is then calculated in equation 42.

$$Q_L = \dot{m}[\frac{\bar{C}_{p,F}(T_\infty - T_s)}{B_T} - L(T_s)] \tag{42}$$

A.3. The Empirical Breakup Model (WERT49)

This model is based on the model of Wert [96], with daya from Hsiang & Faeth [41], Chou & Faeth 1998 [16], Dai & Faeth [23], and Cao et al. [13]. It is presented first by Duke-Walker et al. [24] and later compared to detailed experimental data in [25]. The breakup process is evaluated according to Algorithm 3, where We_{crit} is the critical Weber number for breakup defined in equation 43, and Eo is the Eotvos (or Bond) number defined in equation 44. Note that while We_{crit} is calculated, due to our low Oh it doesnot deviate significantly from 12 (used in other calculations).

$$We_{crit} = 12 \cdot (1 + 1.077 \cdot Oh^{1.60}) \tag{43}$$

$$Eo = \frac{(\rho_p - \bar{\rho_g})\mathbf{a}_p(r_p)^2}{\sigma} \tag{44}$$

The breakup properties are defined when the particle relative velocity reaches a maximum. The We at breakup (Equation 45) and the breakup times (eqns 47 and 48) are then saved and used to calculate the breakup process.

$$We_{brk} = We_{@\tau_{brk}=0} \tag{45}$$

$$t_{brk,c} = \frac{2r_p}{|\mathbf{v}_g - \mathbf{v}_p|}\sqrt{\frac{\rho_p}{\rho_g}} \tag{46}$$

$$\tau_{brk,i} = \min(3, 3.3284(We_{brk} - 12.)^{-0.131}) \tag{47}$$

Algorithm 3 **WERT49 Breakup**

```
STEP 1: Update $Re$, $We$, $We_{crit}$, $Oh$, and $Eo$ since mass/heat transfer changed droplet properties.
STEP 2: Evaluate Breakup
  if $We > We_{crit}$ or $\tau_{brk} > 0$ then
    if $We > We_{crit}$ and breakup has not started then
      → Evaluate/store $|\mathbf{v}_g - \mathbf{v}_d|$
      if child droplet and $Eo < 16$ then
        → Advance to next particle
      else if $|\mathbf{v}_g - \mathbf{v}_p|^n > |\mathbf{v}_g - \mathbf{v}_p|^{n-1}$ then
        → Record current conditions and breakup characteristics (Equations. 45, 47, 48, 13, 46)
        → Advance to next particle
      else if $|\mathbf{v}_g - \mathbf{v}_p|^n < |\mathbf{v}_g - \mathbf{v}_p|^{n-1}$ then
        → Start breakup at the recorded conditions
        → Advance to the next particle
      end if
    else if breakup is underway then
      → Update non-dimensional time (Equation 49)
      if $\tau_{brk} \leq \tau_{brk,i}$ then
        → Advance to next particle
      else if $\tau_{brk} > \tau_{brk,i}$ then
        → Update point radius/parcel (Equation 52 and 50)
        if $\tau_{brk} > \tau_{brk,f}$ then
          → Reset the breakup process
        end if
        → Advance to next particle
      end if
    end if
  else
    → Advance to next particle
  end if
```

$$\tau_{brk,f} = \begin{cases} 3.1862800E-09 \cdot (We_{brk} - 12)^6 - \\ 7.7649400E-07 \cdot (We_{brk} - 12)^5 + \\ 7.3804400E-05 \cdot (We_{brk} - 12)^4 - \\ 3.366090E-03 \cdot (We_{brk} - 12)^3 + \\ 0.0700174E+00 \cdot (We_{brk} - 12)^2 - \\ 0.4157980E+00 \cdot (We_{brk} - 12) + \\ 4.79778 \quad \text{for } We_{brk} \leq 76.45 \\ 6 \quad \text{for } We_{brk} > 76.45 \end{cases} \tag{48}$$

Time advances through breakup according to the non-dimensional time accumulation (Equation 49) with the instantaneous parcel number determined by equations 50, 51, and 52. When breakup has completed the final parcel size is determined by mass conservation (Equation 53).

$$\tau_{brk} = \tau_{brk} + \frac{\Delta t}{t_{brk,c}} \tag{49}$$

$$N_p = \min\left(N_{p,i}\left(\frac{N_{p,f}}{N_{p,i}}\right)^{\nu}, N_{p,f}\right) \tag{50}$$

$$\nu = \frac{\tau_{brk} - \tau_{brk,i}}{\tau_{brk,f} - \tau_{brk,i}} \tag{51}$$

$$r_p = (\frac{m_p}{4/3N_p\pi\rho_p})^{1/3} \tag{52}$$

$$N_{p,f} = N_{p,i}(\frac{r_p}{r_{c,f}})^3 \tag{53}$$

A.4. The Kelvin-Helmholtz Rayleigh-Taylor (KHRT) Breakup Model

This model is derived from Kelvin-Helmholtz and Rayleigh-Taylor hydrodynamic stability theory following the work of Beale & Reitz [3], Su et al. [86], and Reitz [76]. The KHRT breakup is carried out as outlined in Algorithm 4. The breakup times and child droplet sizes are defined in 2.4.

A.5. Deformation and Drag Models

Distortion of the droplet is predicted to enable more accurate drag calculation for the parent droplet before breakup. Our method follows that of the TAB model (O'Rourke & Amsden [67]), solving the equation for drop oscillation, eqn 9. The distortion time, t_b, and frequency, ω_b are then given by eqns 54 and 55.

$$t_d = \frac{2}{C_d}\frac{\rho_p r_p^2}{\mu_p} \tag{54}$$

Algorithm 4 **KHRT Break up Implementation**

```
STEP 1: Calculate breakup times and child radius
  if new KH cycle then
    → Calculate for KH ($t_{brk,KH}$, $r_{c,KH}$)
  end if
  if new RT cycle then
    → Calculate for RT ($t_{brk,RT}$, $r_{c,RT}$)
  end if
STEP 2: Generate child
  $a$) KH update
  if $r_p > r_{c,KH}$ then
    → calculate new radius of parent
    → accumulate mass loss ($m_{brk}$) due to KH break
    if mass loss greater than child's mass, $m_{brk} > m_{c,KH}$ then
      → limit $m_{brk}$ , $m_{brk} = min(m_{brk}, 0.5m_{parent})$
      → create new child particle
      → update radius and mass of parent
      → set $m_{brk} = 0$
    end if
  else
    → set new KH cycle, return to step 1
  end if
  $b$) RT update
  if $r_p > r_{c,RT}$ then
    → update RT time ($t_{RT}$)
    if $t_{RT} > t_{brk,RT}$ then
      → update the particle radius using child radius and then parcel conserving mass
      → set new KH and RT cycle, return to step 1
    end if
  else
    → set new RT cycle
  end if
```

$$\omega_b = (C_k \frac{\sigma}{\rho_p r_p^3} - \frac{1}{t_d^2})^{0.5} \tag{55}$$

Then y is calculated using eqn 56.

$$\begin{aligned} y(t) =& We_b + \exp(-t/t_d) \Bigg[(y_0 - We_b) cos(\omega_b t) \\ &+ \frac{1}{\omega_b} \left(\frac{dy_0}{dt} + \frac{y_0 - We_b}{t_d} sin(\omega_b t) \right) \Bigg] \end{aligned} \tag{56}$$

where,

$$We_b = \frac{C_f}{C_k C_b} \frac{|\mathbf{v}_g - \mathbf{v}_d|^2 \rho_g r_p}{\sigma} \tag{57}$$

The constants C_f, C_k, C_b, C_d are 1/3, 8, 1/2 and 5 respectively.

For KHRT the initial distortion and distortion rate for each timestep are taken from the previous time and new distortion and rate are calculated. However for WERT breakup model, droplet deformation is calculated with Equations 58, 59, or 60 for droplets not breaking up, those that will breakup but have not reached their initial breakup time, or those that are currently undergoing breakup, respectively.

For droplets that will not break up:

$$\begin{aligned} y(t) &\approx We_c \\ y(t) &= \mathbf{min}(y(t), 0.5) \end{aligned} \tag{58}$$

For droplets that will breakup but have not reached initiation time:

$$\begin{aligned} \tau_{mod} &= \tau_{brk}/\tau_{brk,i} \\ y(t) &= \tau_{mod}^{3.2} \end{aligned} \tag{59}$$

For droplets undergoing breakup (after breakup initiation time until end of breakup process):

$$\begin{aligned} \tau_{mod} &= 1 - \frac{\tau_{brk} - \tau_{brk,i}}{\tau_{brk,f} - \tau_{brk,i}} \\ y_0 &= \frac{C_f}{C_k C_b} \frac{|\mathbf{v}_g - \mathbf{v}_d|^2 \rho_g r_{c,f}}{\sigma} \\ y(t) &= \tau_{mod}^{7.5} + y_0 \cdot (1 - \tau_{mod}^{7.5}) \\ y(t) &= \mathbf{min}(y(t), 1) \end{aligned} \tag{60}$$

Once the deformation is calculated, the distorted radius and Coefficient of drag is calculated from eqn 61 and eqn 62 respectively where $C_{d,disk} = 1.52$ and $C_{d,sphere}$ is for a non-deforming spherical droplet.

$$r_{p,d} = r_p \left(1 + C_b \cdot y(t)\right) \tag{61}$$

$$C_{d,d} = C_{d,sphere}(1 - y(t)) + y(t)C_{d,disk} \tag{62}$$

The drag calculation with deformation method is outlined in algorithm 5 for the WERT49 breakup model.

Algorithm 5 **Drag Calculation**

```
STEP 1: Compute $Re$, $We$, and $Oh$
STEP 2: Compute drag
  → Find the droplet distortion
    if breakup is not occurring then
      → Use Equation 58
    else if $\tau_{brk} < \tau_{brk_i}$ then
      → Use Equation 59
    else if $\tau_{brk} \geq \tau_{brk_i}$ then
      → Use Equation 60
    end if
  → Find the distorted droplet radius ($r_{p,d}$, Equation 61)
  → Find the distorted coefficient of drag, $C_{d,d}$
  → Calculate scalar drag according to Equation 7
```

B. Thermophysical Properties

This appendix contains the equations necessary to reproduce the thermodynamic properties used in our calculations. Only equation are present here for brevity.

The subscripts used here for properties are: r reduced Pressure and Temperature, c critical, sat saturation, l liquid phase, v saturated vapor, g gas phase (far from saturation), fg liquid to vapor phase change, ref reference point, and mix gas mixture.

$$T_r = T/T_c,\ t = 1 - T_r,\ p_r = p/p_c,\ p_{r,s} = p_{sat}/p_c \tag{63}$$

B.1. n-Dodecane

$$\begin{aligned}&\text{Critical Point: } T_c = 658.1\ [K]\\ &P_c = 1.817E7\ [dyne/cm^2],\ \rho_c = 0.227\ [g/cm^3]\end{aligned} \tag{64}$$

Saturation Pressure

$$\begin{aligned} &p_{sat} = P_c \exp\left(\frac{at + bt^{1.5} + ct^{2.5} + dt^5}{(1-t)}\right)\ [dyne/cm^2] \\ &a = -9.05690607, b = 2.70206311 \\ &c = -5.12967073, d = -4.64271093 \end{aligned} \tag{65}$$

Liquid Density

$$\begin{aligned} &\rho_l = \rho_c 4.11704705^{(1-T_r)^{2/7}} \frac{A + C^{(1.1-T_r)^B (p_r - p_{r,s})}}{A + C(p_r - p_{r,s})} \\ &A = a_0 + a_1 T_r + a_2 T_r^2 + a_3 T_r^3 + a_4 T_r^4 + a_5 T_r^5 \\ &B = 29.1082033,\ C = 0.655429485 \\ &a_0 = 7.11668060 \times 10^2, a_1 = -1.23859657 \times 10^3 \\ &a_2 = -34.1317310,\ a_3 = 5.28315064 \times 10^2 \\ &a_4 = 5.02474672 \times 10^2, a_5 = -4.69704755 \times 10^2 \end{aligned} \tag{66}$$

Dynamic Viscosity, Liquid

$$\begin{aligned} &\mu_l = 1 \times 10^{-2} \cdot 10^{(a + b/T + c \cdot T + d \cdot T^2)}\ [Poise] \\ &a = -7.0687, b = 1253 \\ &c = 0.013735, d = -1.2215 \times 10^{-5} \end{aligned} \tag{67}$$

Dynamic Viscosity, Gas

$$\begin{aligned} &\mu_g = 10 \times (a_0 + a_1/(a_2 - T) + a_3 T)\ [Poise] \\ &a_0 = -1.51085842 \times 10^{-7}, a_1 = 8.53976847 \times 10^{-5} \\ &a_2 = 2.09853273 \times 10^2, a_3 = 1.60776965 \times 10^{-8} \end{aligned} \tag{68}$$

Latent Heat of Vaporization

$$h_{fg} = \left\{ \begin{array}{ll} mT + d, & T < 490\ K \\ a\exp(-bT_r)(1 - T_r)^c, & T \geq 490\ K \end{array} \right\} [erg/g] \tag{69}$$

$m = -5.48906689E6, d = 5.26484806E9$

$a = 4.92E9, b = 0.141718052, c = 0.397026265$

Specific Enthalpy, Liquid

$$\begin{aligned} & h_l = 10^7(a_0 + a_1T + a_2T^2 + a_3T^3 + a_4T^4) + h_{ref}\ [erg/gm] \\ & a_0 = -945.137032, a_1 = 0.755518692 \\ & a_2 = 3.06477171E-03, a_3 = -1.91986381E-06 \\ & a_4 = 1.18627724E-09 \\ & h_{ref} = h_{g,ideal}(T_{ref}) - h_{fg}(T_{ref}) - h_l(T_{ref}) \\ & T_{ref} = 298.15\ K \end{aligned} \tag{70}$$

Specific Heat, Liquid

$$c_{p,l} = \frac{dh_l}{dT},\ h_l \text{from } 70 \tag{71}$$

Specific Heat, Vapor

$$\begin{aligned} & c_{p,v} = 10^7(a_0 + a_1T_r + a_2T_r^2 + a_3T_r^3 + a_4T_r^5)\ [erg/gK] \\ & a_0 = 2.46705241, a_1 = -5.26687435 \\ & a_2 = 11.987829, a_3 = -6.9343584, a_4 = 0.7744294 \end{aligned} \tag{72}$$

Thermal Conductivity, Liquid

$$\begin{aligned} & k_l = 1 \times 10^5(a_0 + a_1T + a_2T^2 + a_3T^3)\ [\frac{erg}{s \cdot cm \cdot K}] \\ & a_0 = 2.21205592 \times 10^{-1}, a_1 = -3.51131797 \times 10^{-4} \\ & a_2 = 2.53191282 \times 10^{-7}, a_3 = -1.14462592 \times 10^{-10} \end{aligned} \tag{73}$$

Thermal Conductivity, Gas

$$
\begin{aligned}
&k_g = 1 \times 10^5 (a_0 + a_1 T + a_2 T^2)\ [\frac{erg}{s \cdot cm \cdot K}] \\
&a_0 = -1.32079557 \times 10^{-2}, a_1 = 6.02153175 \times 10^{-5} \\
&a_2 = 3.49963929 \times 10^{-8}
\end{aligned} \tag{74}
$$

Surface Tension

$$
\begin{aligned}
&\sigma = a_1 \cdot t^{a_2} \cdot (1 - b_1 \cdot t^{b_2})\ [dyne/cm] \\
&a_1 = 60.81482, a_2 = 0.70311853 \\
&b_1 = 1.42680781, b_2 = 5.20228996
\end{aligned} \tag{75}
$$

B.2. Oxygen

Dynamic Viscosity

$$
\begin{aligned}
&\mu = 10\mu_0 \frac{T_0 + S_\mu}{T + S_\mu} \left(\frac{T}{T_0}\right)^{1.5}\ [Poise] \\
&\mu_0 = 1.919 \times 10^{-5}, T_0 = 273\ [K], S_\mu = 139.0
\end{aligned} \tag{76}
$$

Thermal Conductivity

$$
\begin{aligned}
&k = k_0 \frac{T_0 + S_k}{T + S_k} \left(\frac{T}{T_0}\right)^{1.5}\ \left[\frac{erg}{s \cdot cm \cdot K}\right] \\
&k_0 = 2.44 \times 10^3, T_0 = 273\ [K], S_k = 240
\end{aligned} \tag{77}
$$

B.3. Miscellaneous

Oxygen-Dodecane Gas Diffusion Coefficient

$$
\begin{aligned}
&D = 1.8583 \times 10^{-3}\sqrt{T^3\left(\frac{1}{MW_a}+\frac{1}{MW_b}\right)}\frac{1}{p\sigma_{ab}^2\omega_{ab}} \\
&\sigma_a = 3.467[\text{Å}]; \sigma_b = 6.5972[\text{Å}]; \sigma_{ab} = 0.5\cdot(\sigma_a+\sigma_b) \\
&MW_a = 31.99880\ [\frac{g}{mol}]; MW_b = 170.3348\ [\frac{g}{mol}]; \\
&\omega_{ab} = \frac{1.06036}{t_{st}^{0.1561}} + \frac{0.193}{\exp(0.47635 t_{st})} + \frac{1.03587}{\exp(1.52996 t_{st})} \\
&\quad + \frac{1.76474}{\exp(3.89411\cdot t_{st})};\ t_{st} = \frac{T}{\sqrt{e_{a,k_b}\cdot e_{b,k_b}}} \\
&e_{a,k_b} = 106.7[K]; e_{b,k_b} = 454.6768[K]; \\
&p \text{ in } atm \text{ and } D \text{ in } cm/s
\end{aligned}
\tag{78}
$$

Gas mixture properties are calculated according the thermodynamic relations given by Poling [73].

The product species composition is listed in Table 10.

Table 10
Product species composition.

Product Species	MW [g/mol]	X_i	Y_i
CO	28.0104	0.237082	0.286602
CO_2	44.0098	0.127660	0.242473
H	1.00794	0.048632	0.002116
H_2	2.01588	0.054711	0.004760
H_2O	18.01528	0.252280	0.196148
O	15.9994	0.051672	0.035679
OH	17.00734	0.127660	0.093702
O_2	31.9988	0.100304	0.138520

B.4. NASA7 polynomials

NASA7 polynomials are used for gas specific heat, enthalpy, and internal energy (u).

$$
\begin{aligned}
\frac{c_{p,g}}{R} &= a_1 + a_2T + a_3T^2 + a_4T^3 + a_5T^4 \\
\frac{h_g}{RT} &= a_1 + a_2T + a_3T^2 + a_4T^3 + a_5T^4 + \frac{a_6}{T} \\
\frac{u_g}{RT} &= (a_1 - 1) + a_2T + a_3T^2 + a_4T^3 + a_5T^4 + \frac{a_6}{T}
\end{aligned}
\tag{79}
$$

Constants a_1 through a_7 are listed in Table 11.

Table 11
Curve fit thermodynamic data employed for gas phase.

Gas	Coeff	$200 \leq T \leq 1000$	$1000 < T < 6000$
O_2	a_1	3.78245636E+00	3.66096065E+00
	a_2	-2.99673416E-03	6.56365811E-04
	a_3	9.84730201E-06	-1.41149627E-07
	a_4	-9.68129509E-09	2.05797935E-11
	a_5	3.24372837E-12	-1.29913436E-15
	a_6	-1.06394356E+03	-1.21597718E+03
	a_7	3.65767573E+00	3.41536279E+00
$C_{12}H_{26}$	a_1	2.13264480E+01	3.70187925E+01
	a_2	-3.86394002E-02	5.54721488E-02
	a_3	3.99476113E-04	-1.92079548E-05
	a_4	-5.06681097E-07	3.08175574E-09
	a_5	2.00697878E-10	-1.84800617E-13
	a_6	-4.22475053E+04	-5.26984458E+04
	a_7	-4.85848300E+01	-1.61453501E+02
Product	a_1	3.51130539E+00	3.13307394E+00
	a_2	1.48555737E-04	1.67150071E-03
	a_3	1.83147419E-06	-4.97411555E-07
	a_4	-1.53588695E-09	7.15233359E-11
	a_5	4.19375828E-13	-3.86222828E-15
	a_6	-1.41701622E+04	-1.40943130E+04
	a_7	2.35683587E+00	4.18107019E+00